ALMA MATER STUDIORUM · UNIVERSITÀ DI BOLOGNA

CORSO DI LAUREA IN FISICA DEL SISTEMA TERRA

Field campaign data analysis in support of future FORUM and CAIRT ESA missions

Presentata da:
Lorenzo Cassini

Relatore:
Tiziano Maestri

Matricola n°:
0001008031

Sessione unica
AA 2022/2023

Field campaign data analysis in support of future FORUM and CAIRT ERA missions

Lorenzo Cassini

Abstract

This work aims at analysing the measurements obtained from two instruments, FIRMOS and GLORIA, during their employment in the HEMERA ballon campaign in Timmins (Canada) in the period 23-24 August 2022. FIRMOS is a prototype of the sounder interferometer which of the ESA FORUM mission that is going to be launched in 2027, while GLORIA is a simulator of the CAIRT sensor which is candidate for ESA Earth Explorer 11 whose launch is foreseen in 2031-2032.

FIRMOS *(Far Infrared Mobile Observation System)* is a Fourier Transform Spectroradiometer that has been employed in multiple campaign (Belotti et al.2023 [5]) and is designed to support the future FORUM mission as a validation tool in laboratory and open field campaign. This instrument is extremely important for atmospheric studies thanks to his high resolution of 0.25 cm^{-1} in a spectral range that goes from 10-1000 cm^{-1} (corresponding to 10-1000 μm in wave length). FIRMOS can give us a better understanding of absorption mechanism and entity in the Far InfraRed *(FAR)* section of the electromagnetic spectrum which is, at the moment, unexplored from space. The importance of this data resides in a better understanding of absorption mechanism in this spectral window, which can improve $H_2 0$ concentration retrieval, while giving more information about the Earth radiative budget, essential for a better climate modelling and simulation. (see also FORUM web page [10])

GLORIA++ *(Gimballed Limb Observer for Radiance Imaging of the Atmosphere)* is a imaging limb emission sounders operating in the thermal infrared region of electromagnetic spectra (including MID and FAR infrared). This instrument posses a really high spectral resolution of 0.0625 cm^-1 in a window 750-1400 cm^-1 for a total of 11201 channels. GLORIA has been designed for limb observation of the lower-troposphere/upper-stratospher *UTLS* radiance emitted in the FIR spectral band. The purpose of this is a better understanding of climate and dynamical processes that occur in this boundary region. During the HEMERA campaign this instrument has been employed also for nadir observation and this gives us the possibility to test radiative transfer codes for atmospheric retrieval and cloud identification algorithm on a high resolution spatial grid composed by 48 X 128 pixels. (F. Fried-Vallon et al. 2014 [6]; Riese et al. 2014[11])

The first part of this work deals with the geolocation of the GLORIA data. After that the focus is posed on the scene classification which is obtained by the application of the CIC *(Cloud Identification and Classification)* algorithm. CIC (Maestri et al. 2014 [4]) is a supervised machine learning code based on PCA

Principal Component Analyses that is able to perform cloud identification and classification from high spectral resolution data at infrared wavelengths. The CIC code has been recently tested on the identification of cloudy scenes (Magurno et al. 2020 [12], Cossich et al. 2021[13]). The classification method is based on a distributional approach of a similarity index computed from the element of the dataset with respect to the training set made available to the algorithm. Two different versions of the classificator are tested. The first one is the original CIC which exploits a metric based on the evaluation of the information content of a set of spectra through an analysis of the eigenvectors. The second version relies also on an additional metric accounting for a composite method which also uses the information extracted from the eigenvalues of the analysed set of spectra. For the first time, the CIC algorithm is applied to upwelling radiance fields in this configuration. Another novelty is the CIC application to high spatial resolution data from GLORIA++ to perform a soil classification. The exercise is an important test within the studies aiming at improving the initial guess of the geophysical retrieval of future satellite sounders.

The last section of this work describes the application of FARM algorithm, an optimal estimation based retrieval code relying on an innovative forward model $\sigma - FORUM$. $\sigma - FORUM$ is a modify version of the $\sigma - IASI$ code which is a monochromatic fast code for calculating synthetic radiances in the 10-2760 cm^-1 spectral range. The goal of this analyses is to retrieve atmospheric and surface parameters such as: surface temperature and emissivity, and temperature profiles and H_2O vertical profiles.

Contents

List of Figures

List of Tables

9

Figure 1: ESA's list of Earth Explorer missions

1 Introduction

In this brief section the state of the art for earth observation is introduced and a brief discussion about the experimental campaign HEMERA is presented.

1.1 ESA Earth exploration

During the last decades Earth exploration from space as become one of the most important and challenging task. Our impact on the planet is evident as reported from IPCC *(Intergovernmental Panel on Climate Change)* climate change 2023 report [1] and so an always more efficient way to observe our planet is needed to keep track of its changes and human impact on it.

In this frame, ESA has done a lot of work in the last decades to achieve this objective thanks to its FutureEO *(Future Earth Observation)* program. Started in the 2009 with the launch of the first Earth Explorer, ESA has kept expanding its roster of satellites and is going to do even more in the future: at the moment 3 Earth explorers (SMOS,CryoSat,Swarm) missions are still delivering data and others are in program for the next future. This work focuses on two future missions: FORUM, launch scheduled in 2027, and the CAIRT Earth Explorer 11 candidate, whose launch is scheduled for 2031-2032.

FORUM is extremely important for the future of Earth observation since it can pro-
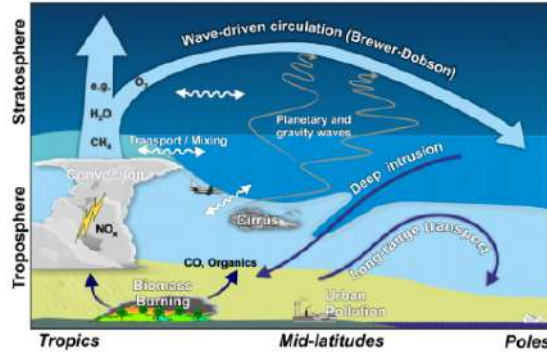
Figure 2: UTLS images Riese et al. 2014

vide data in the Far Infrared part of the spectrum which is unexplored from satellite at the moment. FIR data are already available to us thanks to other experimental campaign such as the REFIR-PAD (*Radiation Explorer in the Far InfraRed*) balloon mission (*Palchetti et al.,2006 [2]*) or FIRST (*Far-Infrared Spectroscopy of the Troposphere*) observation (*Mlynczak and Johnson, 2006 [3]*) and have already proven their utility in the retrieval of clouds optical depths and properties (*M*aestri et al., 2014[4]) and atmospheric state variable such as: temperature profiles, H_2O vertical profiles, surface emissivity (Zhou et al. 2011 [9]) and more. FIRMOS, which has been designed as a prototype of FORUM, has the goal to expand this knowledge and provide a useful tool for data validation and for methods testing. FIRMOS is already been employed in another mission in the Bavarian Alps at Mount Zugspitze, Germany *Belotti et al., 2023 ([5]*) but, thanks to the HEMERA mission, we are know able to analyze its performances in air nadir geometry observation.

For what concerns the Earth Explore 11, at the moment, 4 possible instruments are in pre-feasibility phase; the one we want to focus on is CAIRT (*Changing Atmosphere InfraRed Tomography*) (see also ESA web site [14]). During this mission this instrument, which could be the first limb sounders with imaging Fourier transform infrared technology, is supposed to give a better understanding of the chemical and dynamical processes that happens in the atmosphere between 5 to 120 km altitude. At the moment the closest instrument available that can emulate the results from the CAIRT mission is GLORIA (*Gimballed Limb Observer for Radiance Imaging of the Atmosphere*). GLORIA is designed to observe the UTLS (*Upper Troposphere Lower Stratosphere*) layer and detect dynamical and composition changing through infrared light detection with very high resolution. Its purpose is to fill a gap actually present in the limb observation: the detection of small scale structures and fluctuations under 500 m vertical resolution with a horizontal extent of less than 100 km. GLORIA wants to push this limit down to a 300 m scale in vertical resolution and 30X30 km in horizontal resolution allowing us to

11
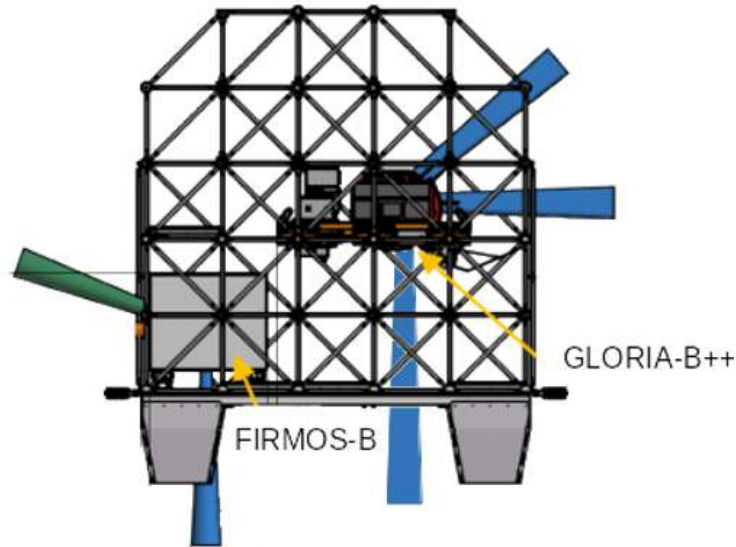
Figure 3: A depiction of the scaffolding in which the two instrument have been installed for the HEMERA campaign

extrapolate a lot of information about UTLS and quasi-horizontal trasport in the LMS (*Lowermost Stratosphere*) (*Friedl-Vallon et al., 2014* [6])

1.2   HEMERA campaign

The HEMERA campaign in which FIRMOS and GLORIA have been employed has been settled in Timmins, Canada in the period 23-24 Aug. 2022. The campaign objective was to test for the first time the performances of FIRMOS for nadir observation and GLORIA for limb and nadir observation. This is an important step for a correct validation of the automatic cloud identification algorithm that are going to be implemented on the FORUM mission. At the same time, the GLORIA instrument has been tested with the purpose to analyse GLORIA performances while also exploiting some of the possible FORUM-IASI synergies. The two instruments have been integrated into a cabin structure and lifted with a stratospheric balloon. During the flight both instruments have taken measurement keeping their FOV aligned with each other by exploiting the laser beam integrated in FIRMOS for interferometric alignment.
During the flight the FIRMOS instrument experienced some issues with a compressor utilized in GLORIA. In detail, the vibration have propagated within the support structure and have altered the optical path within the FIRMOS' interferometer corrupting the measurements. As a results, a lot of the measurements have been declared unusable and only the 12% of the total could be successfully processed and analyze. The FIRMOS

Sequence	N. of level 1B spectra	Start time UTC	End time UTC	altitude Km	sky
F1002	33	18:36:55	18:46:08	13.4-15.5	clear
F1007	32	19:53:07	20:02:20	32.6-34.3	mix
F2002	34	20:46:55	20:56:08	36.6-36.6	cloud
F2009	34	22:33:36	22:42:49	36.1-36.0	cloud
F2011	34	23:04:05	22:13:18	35.5-35.5	cloud
F2012	34	23:19:19	23:28:32	35.4-35.1	cloud
F2013	34	23:34:34	23:43:47	35.0-34.9	cloud

Table 1: Description of the data utilized for level 1C analyses

measurements are organized in several different views, in particular:

- 4 HBB (*Hot Black Body*) views necessary for calibration purposes;

- 4 CBB (*Cold Black Body*) views necessary for calibration purposes;

- 4 limb measurements which have been supposed to be a third calibration source. Unfortunately, due to the noise caused by vibration this data have been corrupted and can not be utilized;

- 34 nadir views in the period 18:36:55 to 23:43:47.

The instrument has been configured before the flight to perform a measure every 16 seconds with a whole sequence lasting about 15 minutes.

GLORIA during the flight haven't experienced any issue due to noise and measurements have been taken successfully during the all flight. The instrument nadir observation have been tested for the first time during this flight. Before GLORIA has been employed only during aircraft flight (Riese et al. 2014[11]). During the flight the instrument has acquired correctly data from the 19:02:01 Aug. 23 2022 to the 08:33:47 Aug. 24 2022. During this period GLORIA was able to obtain a total of 441 granules, 50% of them have been taken in between the 19 and 21 and the rest in the following hours. During the flight the balloon experimented some issues which has caused a progressive lost of height and a progressive descent. This seems to have no impact on the data quality which has kept really high during the whole campaign.
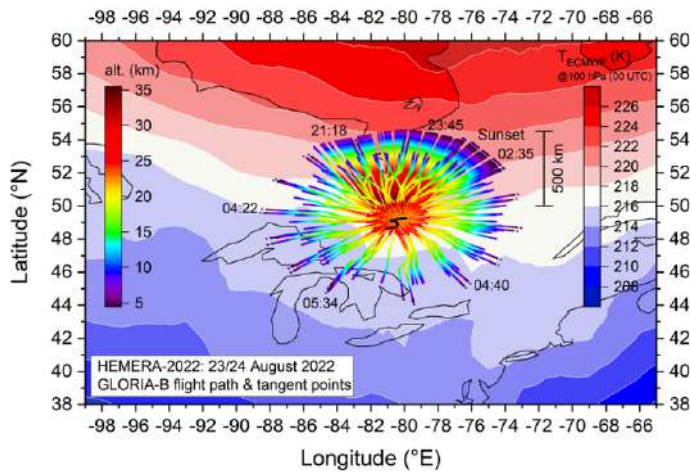
Figure 4: Maps representing the GLORIA path (black line) and tangent points (left color bar) centered in Timmins, Canada. The background represent the ECMWF analyses temperatures at 100 hPa (right color bar)
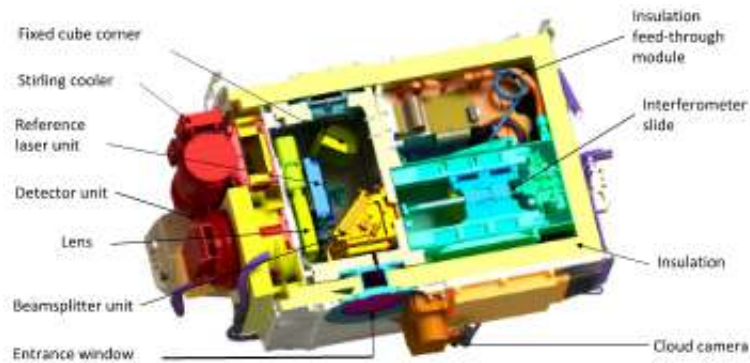
Figure 5: Schematic representation of GLORIA in its different components (Vallon et al. 2014)

2 Instrumentation technical notes

2.1 GLORIA

GLORIA is a IFTS (*Imaging Fourier Transform Spectrometer*) operating in the FIR and MIR section of the spectra. The choice behind a IFTS instead of a traditional FTS resides in the necessity of a high 3D spatial resolution and at the same time, having a compact entrance aperture while keeping a high temporal sampling. Since we're interested in retrieval of gas abundance in the air column, the builders adopted a HgCdTe-LFPA detector in an array of 256X256 adjustable as necessary for the specific campaign. Thanks to this spectrometer GLORIA is able to observe the spectral window from 750 cm^{-1} to 1400 cm^{-1} delivering information about absorption of H_2O, methane
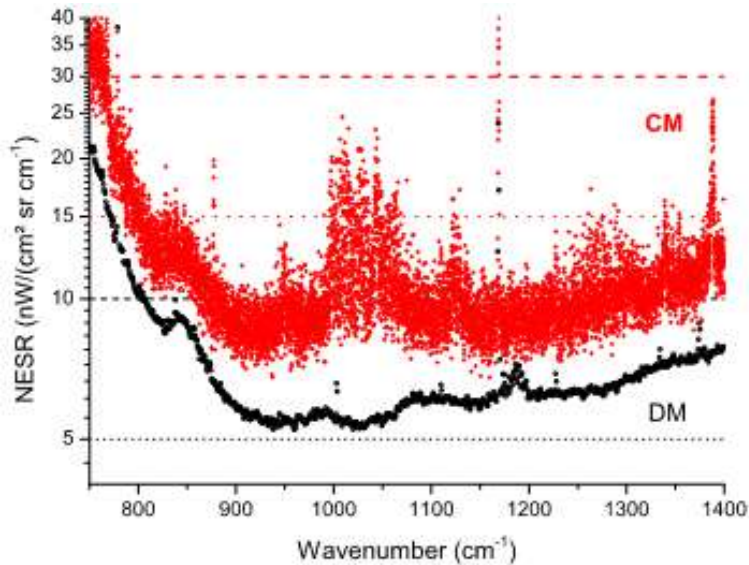
Figure 6: Sensitivity analyses for a calibration sequence made in 26 september 2012. The black dots represent the NESR (*Noise Equivalent Spectral Radiance*) for L1 analyses of a statistic of 43 real black body spectra. The red crosses show the mean NESR for one deep space measurement based on a statistic of the 128 dectors' rows (Vallon et al. 2014).

(CH_4), CO_2, O_3 and others. Also, the necessity to obtain information in a significant fraction of the atmospheric column has lead to a angular opening of -3.3° below local horizon to 0.8° above local horizon while the horizontal spatial coverage is of 1.5°. Gloria is a Gimbal spectrometer with 3 degrees of freedom (yaw,pitch,roll) which helps in the stabilization of the instrument without relying on more complicated optics with longer optical paths and larger optical elements.

GLORIA specifics	DM	CM
spectral coverage	780-1400 cm^{-1}	750-1400 cm^{-1}
spectral sampling	0,625 cm^{-1}	0.0625 cm^{-1}
sensitivity NESR	$< 10 \ nw(cm^{-1}srcm^2)^{-1}$	$< 30 \ nw(cm^{-1}srcm^2)^{-1}$
interferogram length	1.2 s	12 s
temporal sampling	2 s	12.8 s

Table 2: Specific of GLORIA instrument (Vallon et al. 2014)

The instrument has two distinct large area high precision black bodies that are used for calibration when is needed. The instrument can also redirect the center of its FOV to acquire deep space spectra that can be used as an additional source for calibration
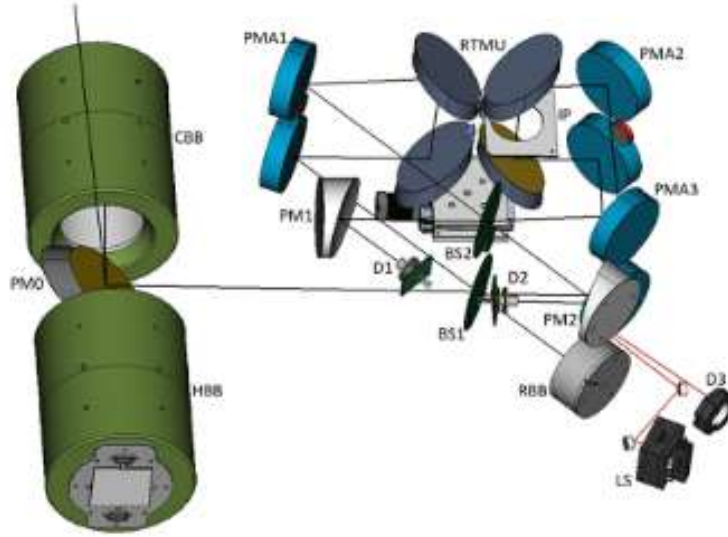
Figure 7: Schematics of FIRMOS optics (Belotti et al. 2023)

after removal of atmospheric emission lines. Spectral calibration is performed every 30-45 minutes to compensate thermal drifting of the optics ($1\ kH^{-1}$). The process requires to evaluate the position of the CO_2 absorption line in between $940 - 972cm^{-1}$ where atmospheric clouds effects are less impactful. Thanks to the calibration system is also possible to measure the NESR (*Noise Equivalent Signal Ratio*) of the instrument for both CM and DM mode. The results are presented in the figure 6. GLORIA can acquire data with two different mode:

- Chemistry Mode (CM) is designed to have a better spectral resolution of 0.0625 cm^{-1} while giving up some spatial resolution and longer temporal sampling. This allows to keep track of trace gases in long range transport mechanism in the UTLS while also observing gaseous folds and filaments inside the UTLS itself;

- Dynamic Mode (DM) has a reduced spectral resolution of 0.625 cm^{-1}, making it worse for gaseous species detection, but has an increased horizontal resolution. This characteristics makes it ideal for observation of dynamical process such as gravity waves' excitation and propagation, Stratosphere-troposphere exchange and convection or quasi-horizontal transport.

.

2.2 FIRMOS

FIRMOS is a FTS *Fourier Transform Spectrometer* operating in the MIR and FIR range, the designed is based on the previous REFIR-PAD but with some updates to make it more easley transportable. FIRMOS interferometer is composed by a double-input and double-output Mach–Zehnder configuration that covers a spectral range of 10-1000 cm^{-1}. The two inputs have different purposes: the first one constantly looks to the scene, the second one is pointed to a Reference Black Body (RBB) that is kept always in thermal equilibrium with the other optical component. The beam splitter (BS) unit is a agermanium-coated biaxially- oriented polyethylene terephthalate (BoPET) which cause degradation of the images after the 1000 cm^{-1} and impose an upper cutoff after this wave number. The acquisition process is perform via room temperature deuterated L-alanine doped triglycene sulfate (DLATGS) pyroelectric detectors with a precision at best of 0.25 cm^{-1}. The scan is performed with a lightweight and compact linear stage model that has a scanning speed of 0.25 mms^{-1}, a single scan requires 16-60 s. The desired radiometric accuracy is obtained thanks to a calibration mechanism that involves 3 black body: a Hot Black Body (HBB), a Cold Black Body (CBB) and a Reference Black Body (RBB) already described. A rotating mirror is located in the interferometer first input and can select either CBB, HBB or the incoming scene's radiance. The two black bodies, HBB and CBB, are essential also for the computation of the instrument's NESR. After the calibration processes, we can compute the NESR as:

$$NESR = \frac{\Delta S}{F} \sqrt{\frac{1}{N} + \frac{2}{n} \left(\frac{\overline{S}}{\overline{S_H} - \overline{S_C}} \right)^2} \tag{1}$$

where: ΔS is the detector noise (random error component) which can be estimated through the standard deviation of a series of uncalibrated measurements of the same source, such as HBB for example, F is a wave number dependent response function, N is the number of scenes acquired, $\overline{S}$ is the average of the spectral information of the N scenes acquired, $\overline{S_H}$ and $\overline{S_C}$ are the average of n measurements of, respectively, HBB and CBB. The results of this computation are represented in the figure 8.

FIRMOS specific	
spectral coverage	10-1000 cm^{-1}
spectral sampling	0.25 cm^{-1}
sensitivity NESR	computed with the equation 1
interferogram length	16 s
temporal sampling	16 min

Table 3: FIRMOS specifics
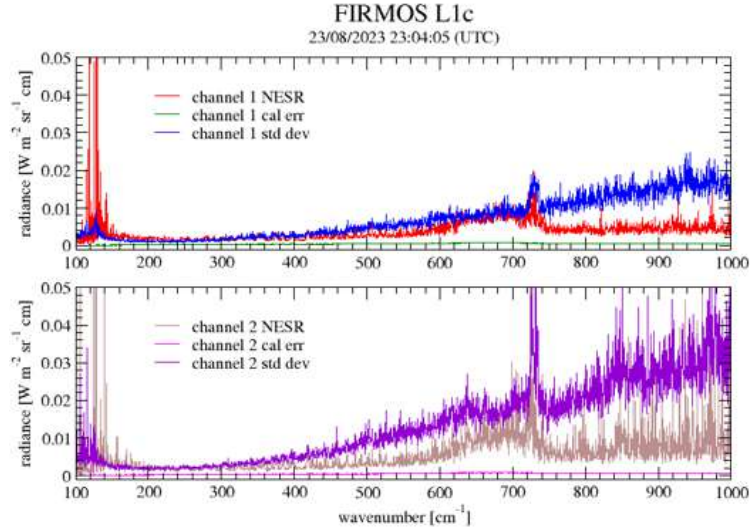
Figure 8: Firmos L1c products NESR, calibration error and standard deviation for both channel 1 (top), channel 2 (bottom)

2.3 L1 data analyses and calibration

2.3.1 GLORIA

GLORIA's data require a post processing after their acquisition before performing any application on them. The first step is the reconstruction of the IR spectrum for each pixel on a common spatial and equidistant grid which is performed with a Brault's interpolation ([7]). After that, a non-linearity correction is performed based on a common correction curve which has been derived in laboratory testing. The computation of the instrument gain function is also necessary and can be done thanks to the calibration measurements: deep space spectra give a first guess for the spectrometer gain which is then corrected based on the cold black body radiation. The final product is obtained utilizing the calibration approach in the complex plane (Revercomb et al. 1988 [15]) and applying to it a bad pixel selection mask. This has the purpose to eliminate pixels with a radiometric gain error bigger than 1.5%. During the analyses the spectra have been apodised with a Norton-Beer strong function.

2.3.2 FIRMOS

The post processing for the FIMROS instrument is divided into 3 main stages:

1. L1a operates a signal conditioning (filtering, detector response compensation, path difference computation) and the Fourier transform operation;

18

2. L1b focuses on the calibration procedure for each spectral channel;

3. L1c compute the mean spectral information in each channel for each acquisition cycle. After this, we end up with two average spectrum, one for each acquisition output, and a third one which is computed as the mean of the two channels; this value is reported with its own associated noise and calibration error. The average are weighted by each measure respective noise.

In FIRMOS dataset each output signal, $S(\sigma)$ where σ represent the wave number dependency, can be written as the difference between two input signals multiplied by an appropriate complex response function F. F, to be as generic as possible, is itself wave number dependent. Under these conditions where able to relate the uncalibrated complex spectrum $S(\sigma)$ with the other quantities thanks to the following relation:

$$S(\sigma) = F_1(\sigma)L(\sigma) - F_2(\sigma)B_\tau(\sigma)$$ (2)

where $L(\sigma)$ represent the calibrated spectrum, F_1 and F_2 are the calibration function and B_τ is the black body spectral radiance of the RBB computed with the Planck formula. The calibration function F can be obtained thanks to a two point radiometric calibration procedure where the input signal is changed from the external scene to the two reference black bodies in sequence for an entire measurement cycle. After this, the calibrated spectral radiance $L(\sigma)$ can be computed reversing the equation 2 and taking only the real part of it:

$$L(\sigma) = R\left[\frac{S(\sigma)}{F_1(\sigma)} + \frac{F_2(\sigma)B_\tau(\sigma)}{F_1(\sigma)}\right]$$ (3)

3 Methods

3.1 L2 data analyses: CIC classifier

In this section i present one of the main tools that have been utilized during the successive analyses which is the Cloud Identification and Classification algorithm (CIC). CIC is going to be the main classifier for the future FORUM mission so having the possibilities to test its performances with real nadir observation is the FIR is really important. CIC is based on PCA (*Principal Component Analyses*) and the criteria for classification are presented in the section 3.1.2 and 3.1.3 which describe two different version of this algorithm:

- the first (Singol Metric) is a more classic approach, which is already been tested on simulated spectra (Maestri et al. 2019[4]) and on data available in the Antartic plateau thanks to the REFIR-PAD instrument. The method rely only on the computation of eigenvector of covariance matrix and their variation;

- the second one relies on more information and implement in the classification criteria also the eigenvalue which are computed during the PCA analyses but have no application in the previous method.

3.1.1 PCA analyses

The Principal component analyses (PCA) is a data reduction technique highly utilized in atmospherics studies. The main goal of this methods is to reduce the dimension in a given data set identifying some new elements, which are the Principal Components (PC), that carry the most of the information about the all data set. These new elements are linear combination of the original data and are built following these criteria:

- the new variables are uncorrelated with each other;

- the new variables preserve all the variance from the original dataset;

- they' re ordered from the one containing the most variance, which is the first, to the one that contains the least, which is the last.

With this constraints we can select only a few of the first PC and be sure that the most of the variability in the original dataset is carried from this few PC, while also reducing the noise in the measures which is contained in the last eigenvectors. The full information contained in the original dataset can be fully preserved only if all the PC are considered. Usually, a common procedure to perform a PCA starts with the normalization of the all dataset since PCA can be performed only on normally distributed variables with mean equal to 0 and variance equal to 1. After this, the covariance matrix in between the

20

original data is computed and the eigenvectors decomposition of it is performed. If X is the original data matrix nxp, where n is the dimension of a single observation and p the number of observation performed, we could write, thanks to the eigenvectors matrix, the PC matrix as $PC = X \cdot A$ where A is the matrix containig the eigenvectors as columns and sorted in the correct way.

3.1.2 CIC algorithm description with single metric

The cloud identification and classification algorithm CIC is a supervised machine learning algorithm based on the already described PCA analyses. This algorithm is designed to be fully independent from the instruments on which is applied and to be, once the training procedure is completed, fully automatic. The method is supervised since a input from the user is still needed in the training phase. In particular, the choice of the number of classes and the construction of the relate training sets has to be done from the users. To keep the approach to the classification mechanism as simple as possible, we suppose to have only two classes: clear sky (TR_{clear}) and cloudy sky (TR_{cloud}) with the respective training set, each one is composed from a certain number of spectra which, in the most general case, can have different dimensions. For each training set a PCA reduction is performed, next the eigenvectors are stored in two separated matrix ($TREM_{clear}, TREM_{cloud}$). The testing phase starts creating two extended training sets obtained by adding a single spectra at the time to both TR_{clear} and TR_{cloud}, the result is a new matrix with one more column:

$$ETR_{Clear} = |TR_{clear}||testspectra| \qquad ETR_{cloud} = |TR_{cloud}||testspectra|$$

Now, if the eigenvectors and eigenvalues are computed once more, we expect different results based on the type of information added to the training set. If the added spectra is from a clear sky scenario, the PCs of ETR_{cleasr} should be almost the identical to the TR_{clear} PCs since no extra information is added to the training set. On the other hand, PCs computed from ETR_{cloud} should be significantly different from the others computed from TR_{cloud}. This shift in the principal component can be computed and utilized as a classification tool: small changes in PCs implies a good agreement between the test spectrum with the corresponding training set, while huge changes in PCs implies a different type of spectra is added to the training set. The classification tool that is used inside the code is a new variable called SI (*Similarity Index*). The SI is a two index characteristic value associated to each test spectra and the other to class that is been tested:

$$SI(i,j) \qquad i \in 1,2 \qquad j \in 1,..,J \tag{4}$$

where i is the number of training set utilized for the classification, J is the total number of test spectra to be classified.

Mathematically, the value SI is computed as follow:

$$SI(i,j) = 1 - \frac{1}{2P_0} \sum_{P=1}^{P_0} \sum_{\nu=1}^{\nu_{tot}} |\mathbf{ETREM}_{i,j}(\nu,p)^2 - \mathbf{TREM}_{i,j}(\nu,p)^2| \tag{5}$$

- $\mathbf{TREM}_i(\nu,p)$ is the matrix containing the normalized eigenvectors of the i-th training set covariance matrix in row, ν is a index corresponding to the wavelength or wave number and p is an index related to the numeration of the principal component for the i-th training set; it goes from $1,...,P_{max}$ where P_{max} correspond to the total number of PC;

- $\mathbf{ETREM}_{i,j}(\nu,p)$ is the matrix containing the normalized eigenvectors of the i-th extend training set covariance matrix defined as $\mathbf{ETR}_{i,j}(i,t') = |\mathbf{TR}_i(\nu,p)||row_j(\mathbf{TS}(\nu,j))|$ where $t' = 1,...,T_i+1$. T_i is the number of spectra composing each training set;

- ν_{tot} is the total number of channels utilized for the PCA analyses;

- P_0 is the umber of principal component that can be associated to a real physical signal and not to noise. It can be computed through a minimization method applied to the following quantity:

$$IND(p) = \frac{RE(p)}{(P-p)^2} \qquad RE(p) = \sqrt{\frac{\sum_{i=p+1}^{P} \lambda_i}{T_i(P-p)}} \tag{6}$$

After computing all the previous quantities the SI can be evalueted and, since we're using multiple classes, we end up with multiple values of P_0. For consistency, after the training phase, only the minimum P_0 is kept and is used as reference for all the sets. The last step in classification requires an analyses of the SID's distribution. In fact this classifier, in an ideal scenario, should been able to produce two distinguished distribution for the SID. For example, if we're using two classes for the training Clear and Cloud, a test spectra coming from a cloudy scene should generate a huge shift in the PC of the training set clear; this result in a value of SID closer to 0. On the other hand, if we add this to the cloudy training set, the variation in PC is minimal and the related SID is closer to 1. Now, we need a way to evaluate when a given SID belongs to one distribution or to the other, and this can be done thanks to the CSID (*Corrected Similarity Index*). This parameter can be computed thanks to a translation of the original SID:

$$CSID(j) = SID(j) - shift_{opt} \tag{7}$$

where $SID(j) = SID(j, clear) - SID(j, cloud)$ and $shift_{opt}$ is the optimal estimation of the parameter Shift that can potentially forecast the performance of the algorithm. The role of $shift_{opt}$ is to translate the SID distribution such as, following the previous

example:

if $CSDI(j) > 0$, then j $\in$ cloudy spectra

if $CSDI(J) < 0$, then j $\in$ clear spectra

3.1.3 CIC algorithm description with double metric

This method is an expansion of the previously described single metric algorithm and is intended to improve the performances of the single metric metric when this gives unsure or none results. The goal is to utilize some of the information that the routine necessary compute but are not extensively used in the classification process. In particular, this new approach rely also on the eigenvalues that are computed during the eigenvector synthesis. The eigenvalue of the covariance matrix is related to the variance of the training set which, during the PCA reduction, are sorted from the biggest to the lowest. We expect that, after adding the test spectra to the training set, the eigenvalues of the matrix ETR_i should be different from the eigenvalue of TR_i. This is true particularly when the test spectra comes from a class j that differs from i, otherwise the fluctuation is minimal because we didn't introduce new information in the training set. The tool that allow us to compute the shift in the eigenvalue is a SI (*Similarity Index*) computed as follow:

$$SI_{eigVal}(i,j) = \sum_{p=1}^{P_0} \frac{|\lambda_{p,TR_{i,j}} - \lambda_{p,ETR_{i,j}}|}{\lambda_{p,TR_{i,j}}} \tag{8}$$

where $\lambda_{p,TR_{i,j}}$ is the eigenvalue associated to p-th principal component of the training set i, $\lambda_{p,ETR_{i,j}}$ is the eigenvalue associated to p-th principal component of the extended training set i. $SI_{eigVal}(i,j)$ can be seen as a the sum of percentage variation in the eigenvalues that go from 1 to P_0.

If we use this index $SID_{eigVal}(i,j)$ next to the previously described $SID_{eigVec}(i,j)$ we end up with a couple of values for each element in the test set. If we represent this couple of values in a plane, we should end up with two distribution in a bi-dimensional space, exactly in the same way we obtained the two distribution in the uni-dimensional case with just $SID_{eigVec}(i,j)$. At this point is possible to identify a straight line that separates at best the two distribution, this line is the analog of the shift variable in one dimension. At this point the classification is done following the criteria:

- if $SID_{eigVal}(i,j) > a \cdot SID_{eigVal}(i,j) + b$ then j-th spectra is assigned to class 1.

- otherwise j-th is assigned to class 2.

3.2 L2 data analyses: FARM code

FAst Retrieval Model (FARM) is a fast and flexible retrieval code, developed in the context of the ASI FORUM-scienza project and tuned to perform retrieval of atmospheric and surface variables.

The code consists of a set of Fortran 95 routines which are designed to solve the optimal estimation problem, as defined by Rodgers (Rodgers, 2000 [**?**]). FARM is capable to retrieve the atmospheric and surface state from the measurements of a generic instrument. In this work it is used to study the data collected by the GLORIA spectrometer.

In this section we explain the basis for the optimal estimation and how FARM computes it.

3.2.1 Optimal Estimation

The optimal estimation is a well known and widely utilized method to obtain information about a certain state vector x, that contains atmospheric and surface variables. Given a forward problem:

$$y = f(x) + e \tag{9}$$

Where y are the measurements, $f(x)$ represents the forward model and e contains all the uncertainties about the problem. The goal of the optimal estimation is to obtain an estimation for x, starting from a set of observed values y, which, in our case, are the spectral radiances. The link between x and y is the function $f(x)$ which maps a state vector into its corresponding spectral radiance. The function $f(x)$ is a radiative transfer model that describes the interaction between light and the atmosphere. This model is not unique and can be chosen based on the fraction of the spectra under analyses, on the state vector we are using and on the type of interaction we are interested in. With the function $f(x)$ and the state vector x we're able to solve the so called direct problem, in which the radiance at a given height is the output of the model. We are interested in an estimation for the state x given the measurements. This would require the knowledge of the inverse function $f^{-1}(x)$. Unfortunately, due to the ill-posedness of this problem, it is generally not possible to have an explicit form for $f^{-1}(x)$.

The x vector is usually find in two ways:

- Using a statistical inference of its value, in the so called statistical retrival;

- Finding an optimal value for the state x, by minimizing a cost function trough an iterative method.

The mathematical shell for the optimal estimation is the Bayes's theorem:

$$P(x|y) = \frac{P(y|x) \cdot P(x)}{P(y)} \tag{10}$$

where $P(x|y)$ is the probability to obtain a given x given a certain y, $P(x)$ describes our a priori knowledge about x and $P(y)$ is a normalization factor.

When we talk about optimal value, we refer to the value of the state x that maximize the probability $P(x|y)$. If we assume Gaussian distributions for $P(y|x)$ and $P(x)$, the problem is the same of minimizing a cost function of the form:

$$\chi^2 = -ln(P(x|y)) = -ln(P(y|x) \cdot P(x)) \tag{11}$$

An explicit form for this optimal value can be derived from this equation only for linear problems with Gaussian distributed variables and no bias. However, due to the non-linearity of the radiative transfer problem, an iterative method is required. From now on, we discus the iterative process which is the one actually implemented i the FARM code.

3.2.2 Optimal estimation: iterative process

The goal of the iterative process is to find the optimal solution of the inverse problem, x_{op}, given a specific a-priori state vector with mean equal to x_a and its own covariance matrix S_a. The process starts from a initial state x_0 which can be set equal to x_a if no more information are available. The model computes $y_0 = f(x_0)$, then the difference between y_0 and y_{obs} is obtained. This difference (called update) is used to calculate the next step in the y space, which is called y_1. Finally, x_1 is computed exploiting the Jacobian matrix $K = \frac{\partial f(x)}{\partial x}$. This process has to be iterated multiple times to ensure that the solution converges to a stable optimal solution x_{op}. The process can be summarized in:

$$x_{i+1} = x_a + (S_a^{-1} S_e^{-1} K_j)^{-1} K_i^T S_e^{-1}[y - f(x_i, b) + K_i(x_i - x_a)] \tag{12}$$

with S_e equal to the effective measurement uncertainty. A graphical representation of this method is presented in figure 9.
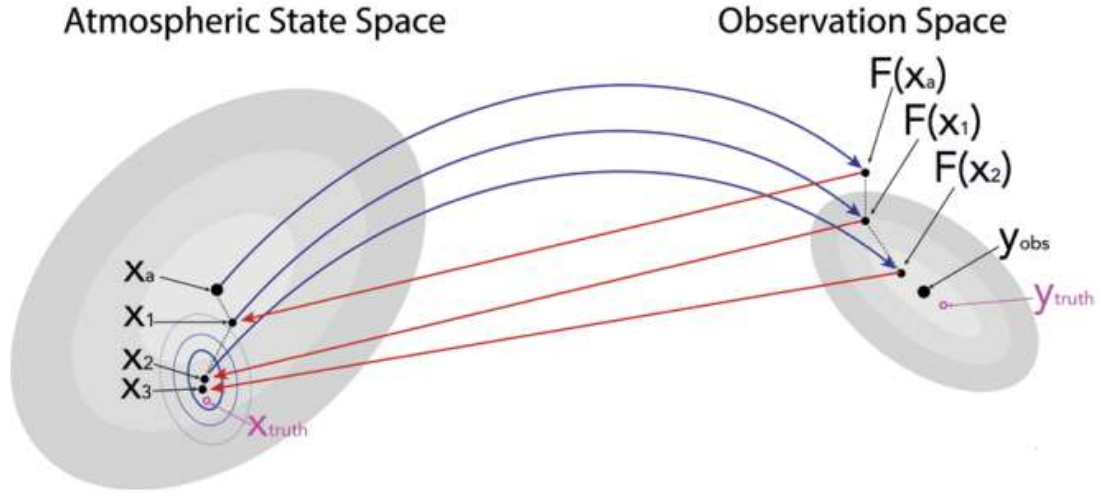
Figure 9: Optimal estimation principle: The ellipses show the (left) prior state and (right) measurement uncertainty.

The iteration stops when a convergence criteria is reached:

$$(x_i - x_{i+1})^T S_i^{-1} (x_i - x_i + 1) \ll length(x) \tag{13}$$

where $S_i = (S_a^{-1} + K_i^T S_e^{-1} K_i)^{-1}$.

An estimation of the quantity of information that can be retrieved can be obtained from the so called Averaging Kernel, which is defined as:

$$A = (S_a^{-1} + K_i^T S_e^{-1} K_i)^{-1} K_i^T S_e^{-1} K_i \tag{14}$$

It is possible to prove that the trace of the Averaging Kernel, $tr(A)$, is equal to the measurement degrees of freedom that characterize my estimation of the state x.
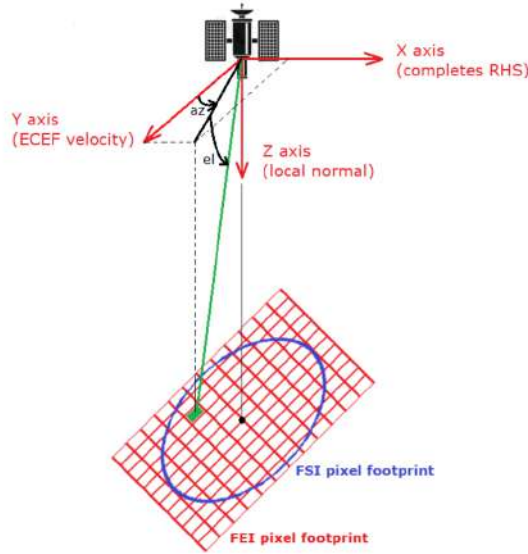
Figure 10: Representation of the instrument pixels azimuth angle (az) and elevation angle (el).

4 CIC analyses and results

In this section the results of the L2 data elaboration computed with the CIC algorithm are presented for both cloud identification and classification and for the innovative soil identification. The following results have been obtained only from the GLORIA dataset which is composed as follow:

Table 4: Number of granules collected at each hours.

h	19	20	21	22	23	00	01	02	03	04	05	06	07	08
#	146	73	16	16	16	11	33	33	25	16	16	16	8	16

Each granule obtained from the instrument is stored in NCDF format. Available data have passed a calibration procedure and a quality check: a bad pixel mask has been applied as described in section 3.1.1. During the period of observation which goes from 23 August 2022 7 PM to the 24 August 2022 8 AM GLORIA performed both nadir sounding, looking at the surface, and a limb observation looking at the horizon, excluding the contribution of the soil. This last measurement mode is not tested here and is excluded from the following analyses.

4.1 FIRMOS data

In this first section is explained for which reason in the following analyses FIRMOS spectra have never been utilized. As explained in section 1.2 about the HEMERA campaign, the FIRMOS measurements experienced some issue during the flight due to vibrations produced by a compressor implemented for the right operation of GLORIA. This caused a very evident contamination in the FIRMOS spectral radiance data set which is still under exam from the ESA campaign team. This contamination seems to have still important effect on some level 2 analyses and for this reason an update versions of the FIRMOS dataset is releasing in mid October to adress this issue.

4.2 GLORIA B++ dataset geolocation

Each GLORIA's granule is composed from an array of $128X48$ pixels, each pixel providing its own spectral information and zenith, azimuth coordinate (respectively yaw and pitch in the dataset) with associate error. The granule's data contains also other information such as: latitude and longitude of the satellite with respect to ecef reference system, altitude of the balloon with respect to ecef reference system, and others variables that have not been utilized during the analyses. To obtain the correct collocation of the image a projection is performed: knowing the elevation of the instrument h and the angular coordinates az (yaw) end el (90°- pitch) is possible to obtain the coordinate with respect to the ENU plane (East, North, Up reference):

$$d = h \cdot \tan(90 + el) \tag{15}$$

$$\begin{cases} d_x = d \cdot \sin(az) \\ d_y = d \cdot \cos(az) \end{cases} \tag{16}$$

Now, from the ENU system, the latitude (lat) and longitude (lon) can be computed thanks to a projection on the Geodetic Reference System 1980 ellipsoid (using the *enu2geodetic* matlab function). This procedure does not introduce any significant errors in the localization since the Hemera gondola flew between $\sim 20 - 30km$ height during the sensor acquisition. The result of this procedure is presented in figure 11.
In particular, in fig 8.c is shown the brightness temperature in the $900~cm^{-1}$ channel, which is an atmospheric window and allow us to see the surface features. We can see that the projection result is consistent with the scene from GoPro images and VIScam (8.a and 8.b) and this confirms the correct location of the scene. Some features such as the street, highlighted from the high values of BT_{900}, are not in the exact position and the overall image posses a small rotation on the horizontal plane. This suggest that there might be an offset in the value reported in the dataset for the azimuth angle: $az_{correct} = az_{real} + \delta$. If we include the presence of this offset, which has been set to 15° in

this image, the result shows a better agreement between the surface and the brightness temperature profile.

After analyzing the most of the data available, we are sure that this offset is present in the most of the images. Its value is different in each image and does not seem to follow any particular pattern until 8:30 PM when the offset is still present but with less fluctuation between images. An explanation of this can be given analyzing the uplift phase of the balloon: as reported from the campaign team the case containing the instrument could have rotated around the vertical axes because of local atmospheric motion; this motion is not detectable from the instrument on board and could have introduced a variable offset in the az angle. This rotation is shown both on the GoPro images and VIScam images.

(a)   (b)
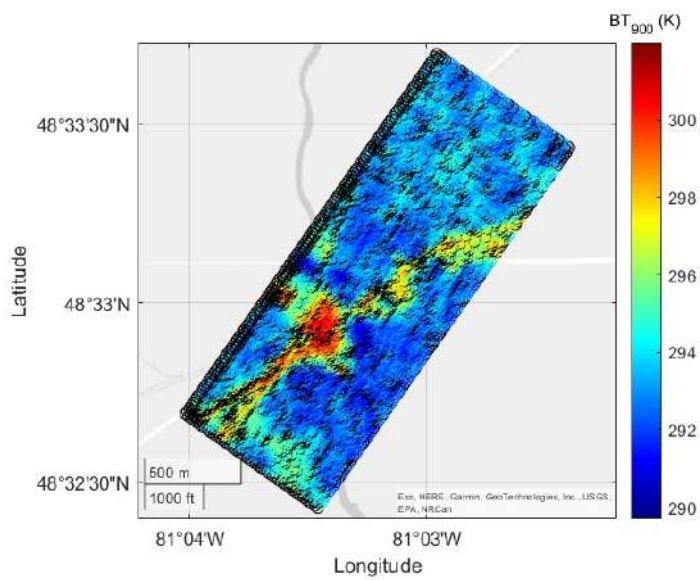
(c)

Figure 11: a) image taken from the on board GoPro at 19:51:20 on Aug. 23, the yellow square represent approximately the granule's area; b) image taken from the VIScam at 19:51:51 on Aug. 23; c) granule collected at 19:51:17 on Aug. 23.
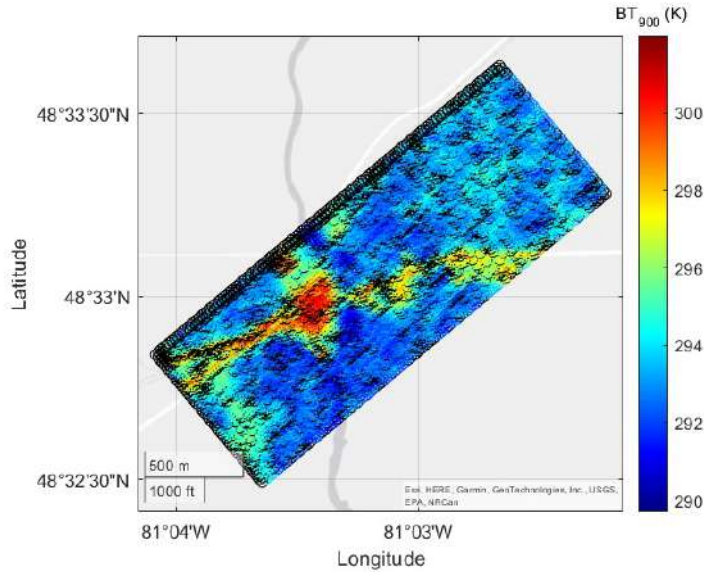
Figure 12: granule collected at 19:51:17 on Aug. 23 with a rotation offset of $\delta = 15$

4.3 CIC classifier for clear and cloudy sky

4.3.1 Training set construction: selection of images and classes

For the CIC classifier to work properly, a test set is needed for each possible sky scenario. To do so it is necessary to identify in our dataset enough images in which the instrument Field Of View (FOV) is looking at a clear sky scene or a cloudy sky scene. This is possible thanks to the information obtained in section 4.1 about the geolocation of each granule combined with the VIScam and GoPro images. As shown in the figure 11 the GoPro, VIScam, and GLORIA granule are not acquired all at the same time, so some discrepancies can be present between data and images.

With this procedure is possible to select a set of images for a clear sky situation and for a cloudy sky situation which is the starting point for test set construction. A simple way to test the accuracy of the selection procedure is the comparison with with a threshold method. In this case the difference of brightness temperature between 2 specific wave number 800,1200 cm^{-1} (Bt_{800}, Bt_{1200}) with respect to the brightness temperature at 900 cm^{-1}(Bt_{900}) are computed. The results are represented in two graphs 13 versus the Bt_{900} values.

This representation shows clearly two separate distribution associated to a clear sky situation (color red) and a cloudy sky (color blue) with difference in brightness temperature of the order of 20 K°. Anyway, the threshold method is not enough to give a correct identification of all the possible scene, in fact:
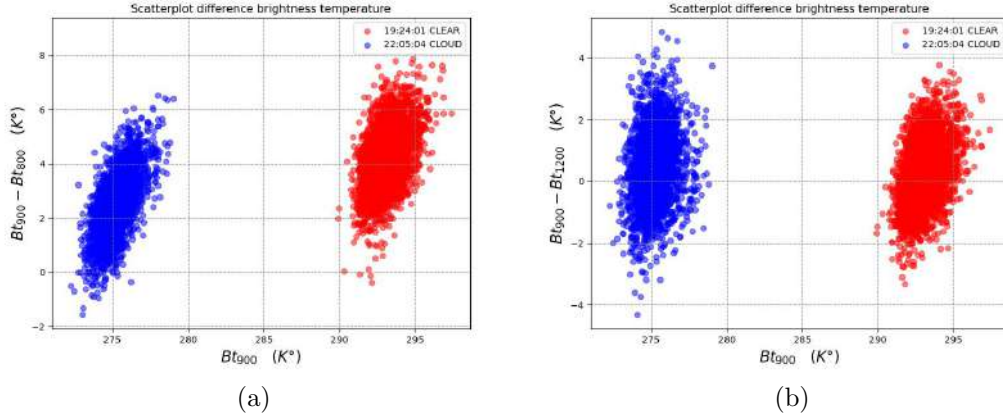
Figure 13: a)This scatterplot shows the difference between the distribution of $Bt_{900} - Bt_{800}$ vs the Bt_{900} values. The red one is for a clear sky situation, the blue for a cloudy sky; b) Same as before but with channel at 1200 cm^-1 instead of 800 cm^-1

- the dispersion of the points within the two cluster, both for clear and cloudy sky, due to the presence of different types of soil in the FOV of the instrument, can't be examined with just the difference in brightness temperature but requires a better analyses that can be done with the CIC classifier itself;

- the separation between the classes is strictly related to the $B_t 900$ and so we can aspect it changes due to variation in the insolation during the day or from season to season,

- in this representation there are a lot of granule that are not easy to identify as cloud or clear because the difference in B_t are in between the two classes (fig.14). In this case is the operator that has to choose which class suited the best, this can be done only if VIScam or GoPro image are available.

For this reasons the threshold method is been applied only during the training set construction and not as an analyses tool for unknown scene where CIC will be preferable. Also, due to the presence of a third class not easily identifiable, has been decided to introduce an additional training set. This third distribution is due to the presence of a thin cloud in the field of view of the instrument as shown both from the VIScam images and from the brightness temperature profile in the granule of interest (fig.15).

To isolate the pixels that are related to this type of clouds a filter on the threshold method has been implemented and applied it on the scatterplot illustrated before. In particular, only the pixels that posses a brightness temperature at 900 cm^-1 in a window of 282.5 K° to 288 K° have been selected in this procedure. This selection is consistent with the geolocation of the thin cloud done with the images (fig.15).
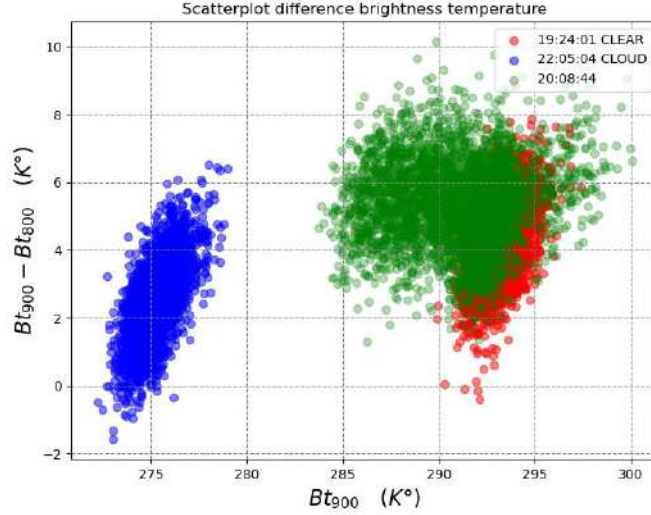
Figure 14: Scatterplot of $Bt_{900} - Bt_{800}$ vs Bt_{900} for three different images

Training set	number of element	period of sampling
clear scene	70	10 granules acquired between 19:00 and 20:00
cloudy scene	28	4 granules acquired between 21:00 and 22:00
	21	3 granules acquired between 22:00 and 23:00
	21	3 granules acquired between 23:00 and 24:00
cirrus scene	70	1 granules acquired at 20:08:44

Table 5: Recap of the granules from which the training set have been constructed

At the end of this process has been possible to identify 10 granule each one containing all clear pixels, 10 granule containing only thick cloud pixel and 1 granule containing thin cloud pixels which have been isolated from the rest of the scene. To build the training sets only 70 pixel have been sampled from the total. In specific:

1. for clear sky and thick cloud sky 7 pixels from each granule have been selected;

2. for thin clouds 70 pixels have been selected in between the all amount of pixels coming from the threshold filter.

The sampling of the pixels within each class has been done randomly since we're not interested in identifying different type of soil in this phase, but only in the difference between clear and cloudy scenes. A more accurate selection of different types of soil is performed in the section 4.3 where CIC performances as soil identifier are tested.

33
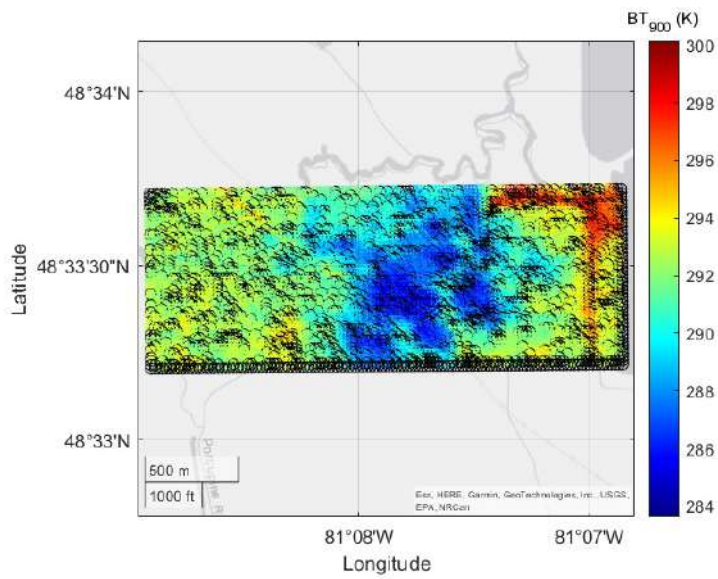
Figure 15: Image taken from the on board GoPro at 20:08:38 on Aug. 23, the yellow square represent approximately the granule's area; b) image taken from the VIScam at 20:08:38 on Aug. 23; c) granule collected at 20:08:44 on Aug. 23.

(a)   (b)
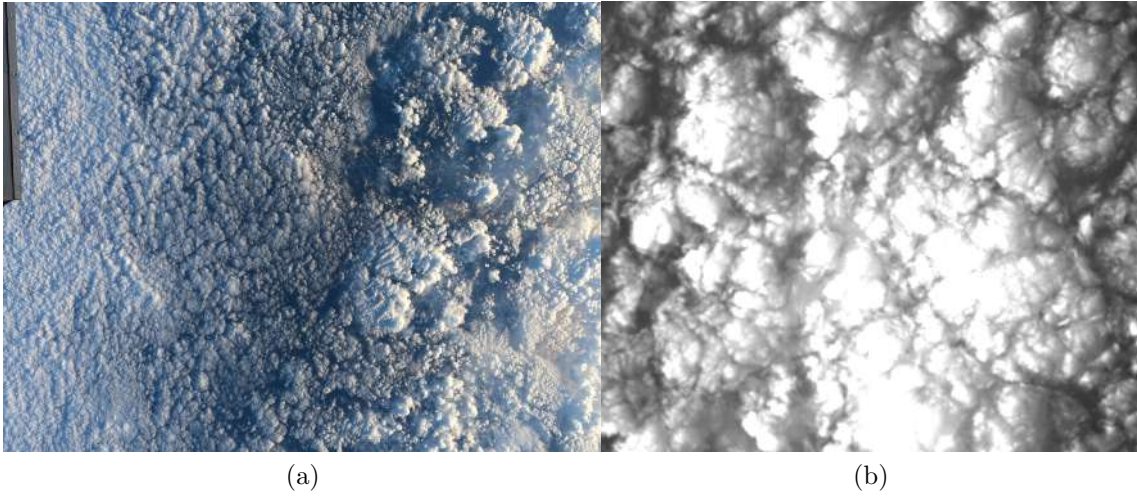
Figure 16: Example of a cloudy sky scenario; a) image taken from the on board GoPro at 23:38:10 on Aug. 23; b) image taken from the VIScam at 23:38:13 on Aug. 23.

To summarize, the threshold method has been used only in training set construction and has been supervised from the operator comparing with the scatterplot results. To reduce as much as possible errors in this first classification only the scenes that can be clearly identified as clear sky, cloudy sky, cirrus cloud with this method have been utilized for the training set's building. After identifying a sufficient number of images or pixels for each class of interest, we've selected 70 pixels that compose the training sets for that specific class.

4.3.2 Spectral channel reduction

Figure 17: Sample mean of all the 70 spectra contained in each training set with the corresponding error (shaded band = 1 σ).

This section describes the spectral interval that have been selected and why such a sampling is necessary. As we can see from the brightness temperature profile display in the figure 17, the difference in between the classes are clear and for the most part exceed by a significant amount the sample error. It's also clear that such a high spectral resolution is able to highlights a lot of features, such as absorption line from different atmospheric component, in which the difference between spectra became barely visible. Since CIC algorithm's execution time depends on the number of channels utilized in the classification a reduction in the spectral resolution is performed. This has the purpose to exclude spectral bands affected by gas absorption and not useful for the classification while also improving the execution time. In particular, have been kept only the wave numbers between 750 to 1000 cm^-1 and 1100 to 1200 cm^{-1} with a sampling of one channel every eight one. The results are shown in figure 18. This areas have been selected since they don't contain any information about the surface or related the cloudds absorption or contribution. The final result also brings the GLORIA' s spectral resolution in line with other instruments on which CIC is already been tested such as PRE-FIRE.
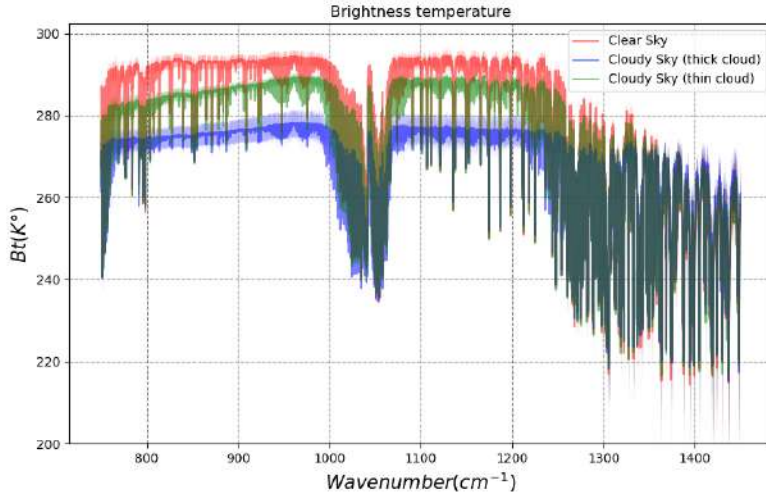
36
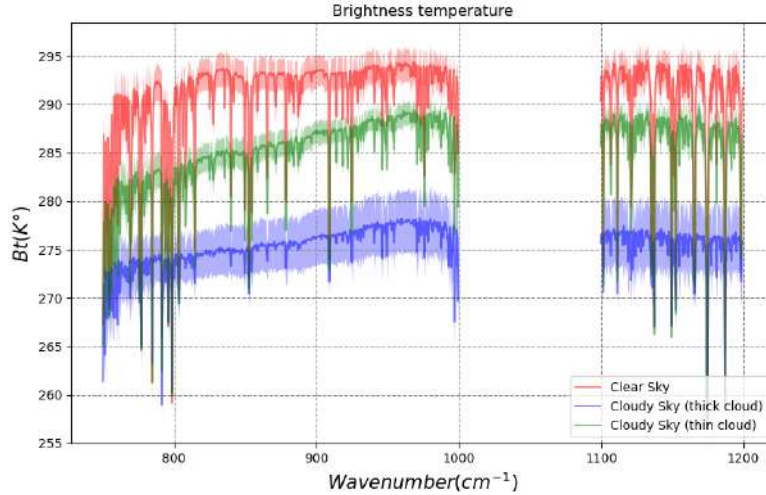
Figure 18: Sample mean of all the 70 spectra contained in each training set with the corresponding error (shaded band = 1 σ) after channel reduction.

With this procedure has deleted for the most part: the contribution of the O_3 which creates a huge absorption line in the band covering the spectral range 1000 to 1100 cm^-1, the continuum absorption from $H_2 0$ after 1200 cm^{-1}. Some absorption lines are still present in the final product but is possible do delete some of them with other selection method discuss in the 4.3.2 section.

4.4 CIC cloud classification results

In this section the results obtained with the CIC classifier on different test set are presented. In particular, 3 sets of images have been tested, each one containing different scenarios. Each test set has different purpose and aims to verify specific skills of the CIC classifier: how the soil composition affects the classification (clear sky), how the algorithm is able to discriminate correctly different types of clouds (cloud test), how different object and shape are resolved from the classifier. With this procedure possible miss classification have been searched and the overall results of the algorithm have been tested. All the following analyses have been done with the CIC classifier with a single metric approach.

4.4.1 Clear test set

This test set is designed to test the abilities of CIC to identify clear scenario with multiple superficial features. For this reason three images have been selected in such a way to

37

(a) (b)
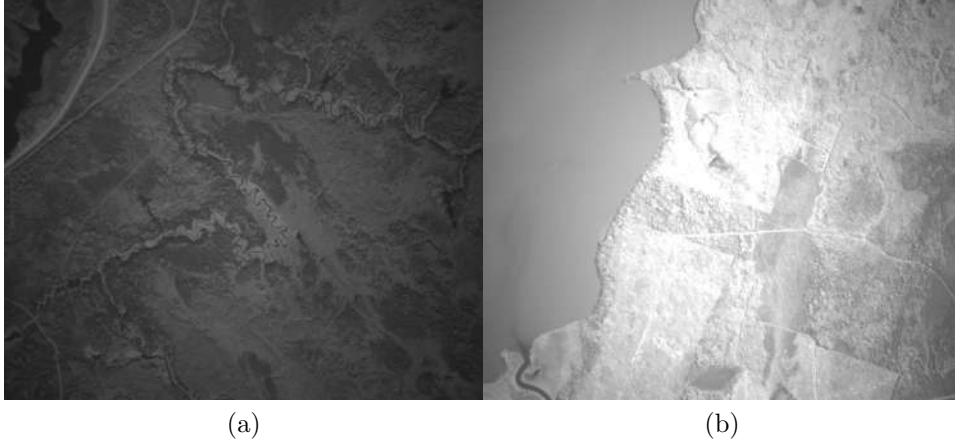
Figure 19: a) Image taken from the on board VIScam at 19:02:22 on Aug. 23; b) images taken from the on board VIScam at 19:17:33 on Aug. 23

Granule	classification		
	clear	cloud	cirri
19:02:01	4646	0	0
19:02:15	4590	0	0
19:17:33	4585	0	0

Table 6: Result given by the CIC algorithm for the clear test set

include different types of soil: a lake, a river, grass fields and forests are analyzed. The images in this test set have been taken at 19:02:01, 19:02:15, 19:17:26.

The result presented in table 8 shows that, for each images analyzed, CIC has reported a 100% of clear pixel in the granules. This is consistent with what the scene looks like from the VIScam and the GoPro and the different surface present in the scene don't affect the result in any way. GLORIA has acquired granules also during night but the VIScam and the GoPro are completely black and is impossible to recognize if the instrument is looking at a clear sky or cloudy sky. For this reason this granules have not been considered during the test.

4.4.2 Thick cloud test set

This test set is designed to verify if the algorithm is able to identify correctly thick clouds and if is possible to discriminate small section of thin clouds in more complex images. The images in this test set have been taken at the 23:37:55, 23:38:22, 00:38:35. As we can see from the results, even in a situation where the sky is completely covered by
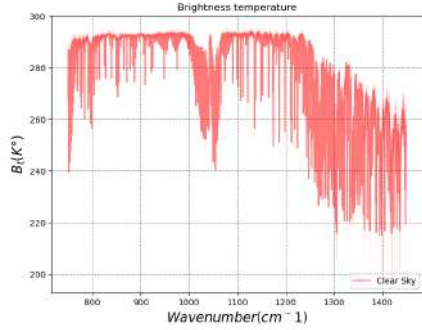
(a)
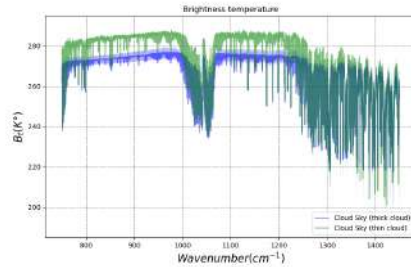
(b)
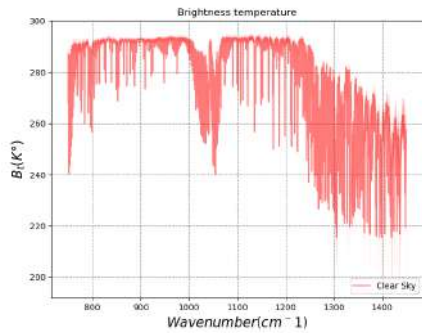
(c)
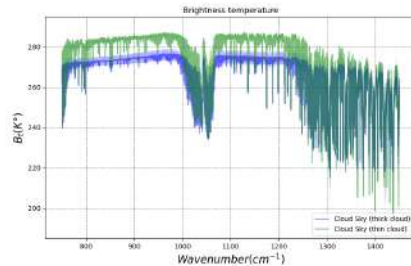
(d)
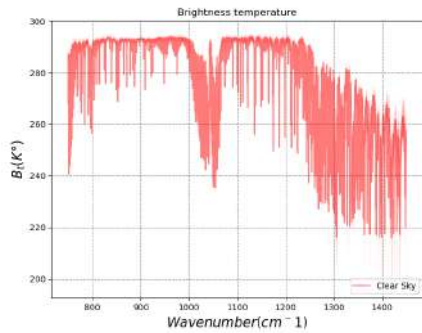
(e)
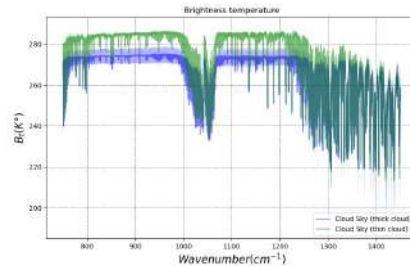
(f)

Figure 20: In the left column: brightness temperature profile $Bt(\nu)$ for each image in the training set clear: a) 19:02:01; c) 19:02:15; e) 19:17:33, with the corresponding error (shaded band = 1 σ). In the right column: brightness temperature profile $Bt(\nu)$ for each image in the training set cloud: b) 23:37:55; d) 23:37:55; f) 00:38:35 with the corresponding error (shaded band = 1 σ).

Granule	classification		
	clear	cloud	cirri
23:37:55	0	2304	7
23:37:55	0	2247	8
00:38:35	0	2409	60

Table 7: Result given by the CIC algorithm for the thick cloud test set

(a)   (b)
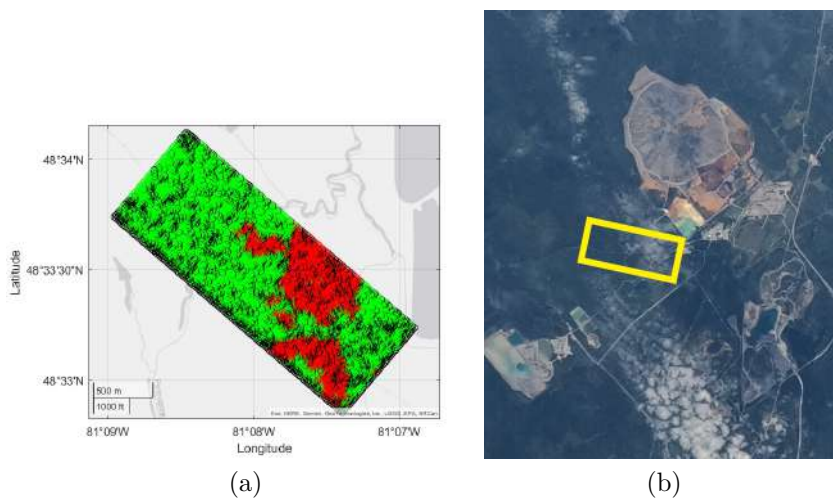
Figure 21: a) CIC classification of the granule collected at 20:09:25: green area is Clear sky, red area is cloudy sky (Thin cloud); b) images taken from the on board GoPro at 20:09:20

thick clouds the algorithm is still able to identify some pixels as cirrus clouds. This seems realistic because, looking at he VIScam, is possible to identify some areas where the cloud cover is thinner. This implies that the optical depths of the clouds is smaller and so more radiation is able to go through the cloud, this variation is detectable with our instruments and methods. A further analysis accounts for the brightness temperature spread of the spectra within each class. The spread is computed as $sigma(\nu) = \sqrt{var(B_t(\nu))}$ and for the thick cloud classification is of the order of 3.36 K° at the 23:37:55, 3.34 K° at 23:38:22, and 4.14 K° at 00:38:35 while the mean difference between the spectra along all the channels is respectively: 6.74 K°at 23:37:55, 6.72 K° at 23:38:22, 7.32 K° and 00:38:35. The difference between the mean spectra are $\approx 2\sigma$ so a miss classification of the algorithm seems unlikely.

Granule	classification		
	clear	cloud	cirri
20:09:11	2842	0	1617
20:09:25	2816	0	1694
20:09:39	3271	0	1141

Table 8: Result given by the CIC algorithm for the thin clouds test set

4.4.3 Thin cloud test set

This third test set is designed to explore the ability of the CIC to identify the shape of some thin clouds that might cover just a fraction of the full instrument field of view. This results are important for different reasons: the ability to discriminate the shape of some object is something never attempted before since the spatial resolution usually doesn't allow an accurate collocation of the clouds, the ability to identify precise shape is fundamental if we want to utilize the CIC as a soil classifier (see next section). The granules utilized for this classification are acquired at: 20:09:11, 20:09:25, 20:09:39. As presented in figure 21 the algorithm is able to picture correctly the shape of the cloud crossing its field of view. In this case given an objective truth for each pixel is difficult since the only comparison is given by the GoPro image which doesn't have enough resolution to discriminate such small details. Furthermore, the difference between the mean spectra in this images is really small ($\approx 1\sigma$) and this suggest that some miss classification might be present bit still the overall result is really good(fig.22).

For this reason a support method has been implemented during this analyses to verify the CIC classification. In our case, a clustering method implementing a k-mean mixture of Gaussian method has been utilized. The only input required from the k-mean are the data and the number of classes we are interested in, then the algorithm sort all the different pixel in one of the three classes which are built maximizing a similarity criteria (Mittal et al. 2021[16])

If the results of the clustering are considered as the truth, the comparison between the 2 classes clustering and the CIC results return an accuracy bigger then 90 % (an exact calculation is still under exam). This proves the accuracy of the CIC methods utilized during the analyses. The introduction of a third class impoverishes the results and introduce an extra alyer of complexity in the image which seems not necessary. It is also important to point out that the clustering method is forced to use three classes even if three classes might not be necessary to classify correctly the image; on the other hand CIC is able to select by itself how many classes are necessary for a correct classification.

41

(a)

(b)

(c)

Figure 22: Mean brightness temperature for each class identified by CIC present in the granule a) taken at 20:09:11 on Aug.23; b) taken at 20:09:25 on Aug.23; c) taken at 20:09:39 on Aug.23 with the corresponding error (shaded band = 1 σ)
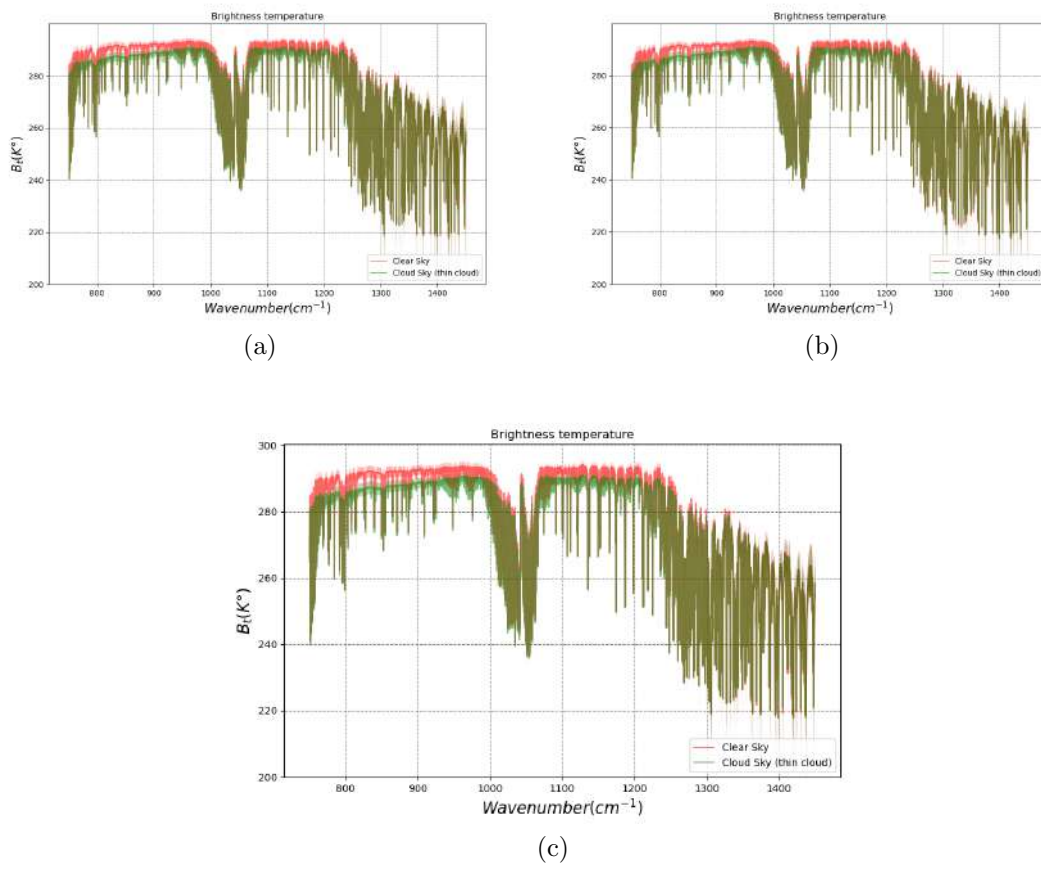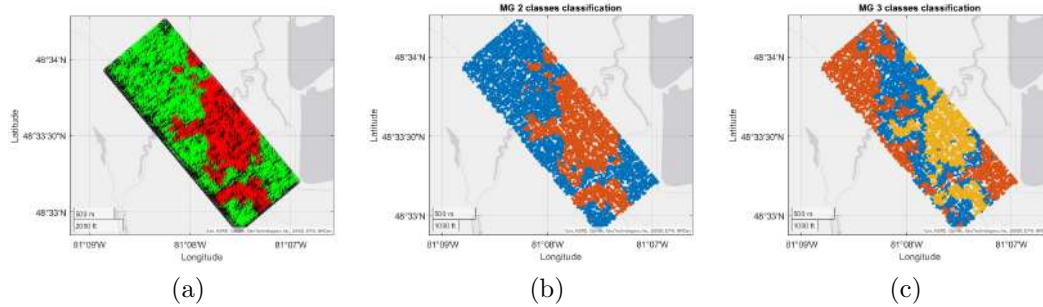
Figure 23: a) CIC classification of the granule collected at 20:09:25 on Aug. 23 where: green section = clear, red section = cirrus cloud; b) Clustering results for the granule collected at 20:09:25 on Aug. 23 whit 2 classes available; c)Clustering results for the granule collected at 20:09:25 on Aug. 23 whit 3 classes available

4.4.4 Additional results

In this section one last interesting result obtained during the testing phase is presented. In this particular image is possible to find all the 3 classes in a single frame as shown in fig.24. This granule has been collected at 20:27:47 and the classification made by the CIC is very consistent with the GoPro and VIScam image. Such a result is really useful for future application of retrieval method since there might be the possibility to identify different optical depths in different section of the same cloud. This can give information about its composition while also its height which is a difficult task to achieve from in air observation.

4.5 CIC classifier for soil classification

In this section the evaluation of the CIC's performances as a soil classifier have been tested. The purpose of this analyses is to see if CIC could be implemented in future mission as a classification tool both for cloud and for the different types of surface. This is the first time trying to utilize CIC to recognize different spectral features of different types of soil. All of this is possible thanks to the high spatial resolution grid available with GLORIA and the different variety of soil observed during the campaign.

4.5.1 Training set construction

As done in the previous section a good training set is needed for the algorithm to develop a correct classification. This time the number of classes has been increased from 3 to 5, this is necessary to take into account all the different types of soil:

1. the class $ACQUA$ (AC) contains 55 pixels from different water sources (deep water
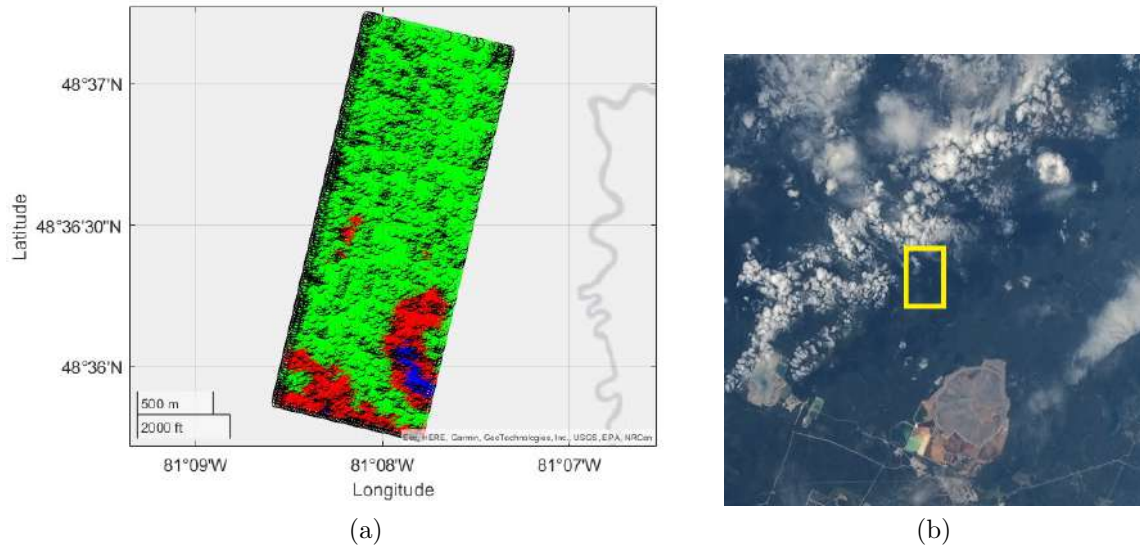
43

Figure 24: a) CIC classification of the granule collected at 20:20:47 on Aug. 23; b) Spectral mean brightness temperature for each class identified by the CIC.
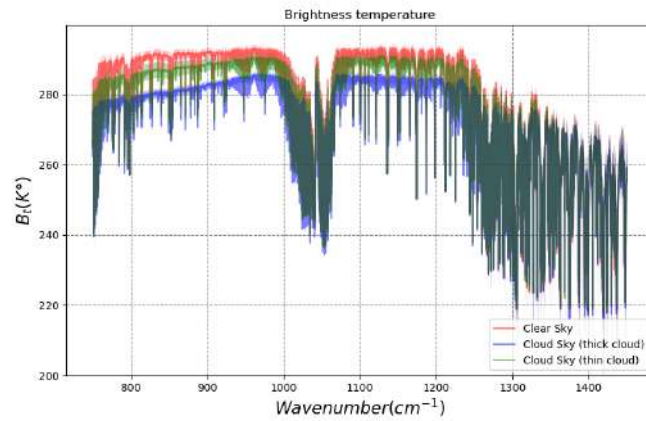

Figure 25: Mean spectral brightness temperature for each class identified by the CIC in the granule collected on 20:27:47 of Aug. 23
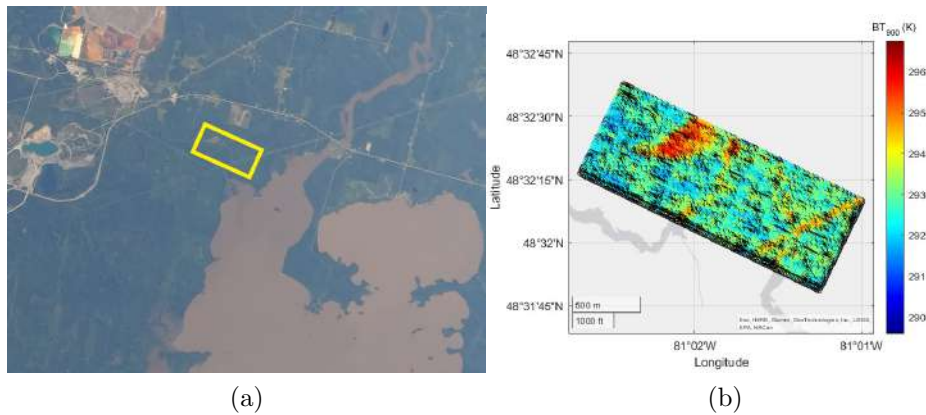
Figure 26: a) GoPro image taken at 19:32:20 on Aug. 23 b) Bt_{900} of the granule acquired at 19:32:21 on Aug. 23

lake, shallow water river and small basins);

2. the class *PRATO* (PR) contains 42 pixels from grass fields or area where no high vegetation, such as trees, are present;

3. the class *ASFALTO* (AS) contains 38 pixels from all different anthropogenic sources such as streets and buildings;

4. the class *BOSCO* (BO) contains 46 pixels from areas where flourishing green vegetation is present such as high trees or wooded areas;

5. the class *SABBIA* (SA) contains 29 pixels from wide areas where vegetation and anthropic presence are absent.

To select these pixel was not possible to use the threshold method as done in the section 4.2.1 because the difference in Bt_{900} don't give us all the information we need. Is possible, looking at the $Bt(\nu)$ profile to recognize some features such as streets or sand, but difference in between different biome are not appreciable with this method. In fact the threshold method utilize only the information contained in two single channel, without taking into account the variation of the all spectra between different classes of surface. Furthermore, it is very sensible to variation between day and night observation, which is something we want avoid since the analyses method should be as generic as possible. To obtain a first guess for the pixels the following method has been adopted: each images after a first localization utilizing the Bt_{900} profile, has been compared to a high spatial resolution RGB map, in our case Google Earth has been used. Only the pixels that are clearly identifiable in one class have been then utilized for the training set. To verify the first guess a clustering method was applied. For this purpose, the

45

Figure 27: a) Clustering results of the granule taken at 19:32:20 on Aug. 23 with 3 classes; b) Clustering results of the granule taken at 19:32:20 on Aug. 23 with 4 classes.

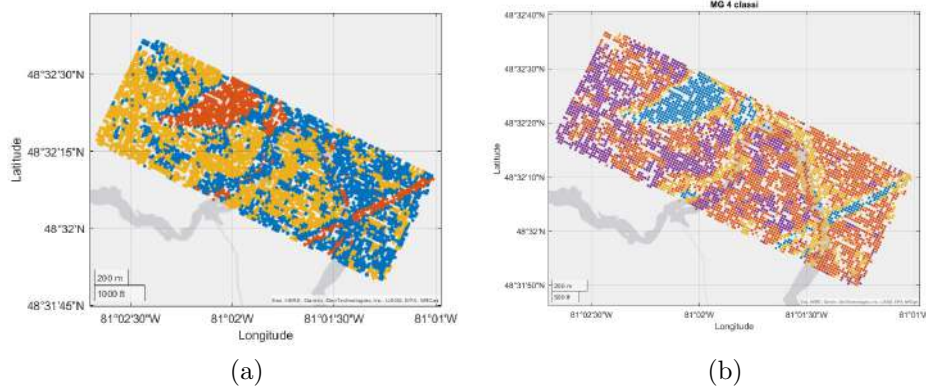same clustering method adopted during the cloud identification has been adopted (non supervised clustering based on mixture of Gaussian k-means method). This procedure provides also the full classification of the granule that can be later compared to the CIC result as a check to evaluate the performances. All the pixels for this training set have been acquired in between the 19:18:48 of Aug.23 to the 20:07:50 of Aug.23.

The figure 27 is an example of the results obtained with the clustering method with three classes available (a) versus a result with 4 classes available (b). The main feature such as the presence of the river, the street on the right or the huge grass field area are all present in both the classification. The 4 class clustering include an extra layer of complexity to scene that might not be needed. In fact, the fourth class was initially introduced to see if the clustering was able to assign a specific class to the street on the right since it's the only anthropic element in the granule. From the results presented here is possible to see that the street is classified a grass field and the fourth class add just more features inside the woods section of the image. For this reason during the testing phase only three training set at a time have been kept, switching in between them as needed. After this a validation test is built to verify the performances of the CIC, assuming the clustering results as an objective truth, partial results are presented in the table 9. As we can see the class PR which represent the grass fields is the most under performing.

4.5.2 Spectral Channel reduction

After the construction of the training set a spectral reduction is performed such as described in the section 4.2.2. In this case, the simple cutoff on the wave lengths in between 1000-1100 cm^{-1} and after the 1200 cm^{-1} plus the sampling of 1 spectra each 8 is not enough to guarantee a reasonable computational time. To improve the selection,

granule tested and classes utilized	N. of pixel	accuracy	miss classification
19:19:02 AC - PR - BO	6	0.667	PR
19:32:21 AC - PR - BO	5	1	-
19:34:10 AC - SA - BO	6	1	-
19:50:22 PR - AS - BO	6	0.833	PR
19:59:13 PR - AS - BO	6	0.833	PR
20:07:50 AC - AS - SA	6	0.667	AS

Table 9: Testing phase results on different classes for CIC as surface classifier

before applying the cut off, some of the absorption lines present in the spectra have been eliminated. This can be done because the absorption line are characterized from the atmospheric' s components and so are completely independent from the pixel on such a small spatial scale. The spectral line are preserved from pixel to pixel so they're still visible in the sample mean of a certain class, but they are smoothed from a sliding mean which is computed taking into account 11 channels not a single one. With a superimposition of a sliding mean to the sample mean, for each class, we can select the channels in which the sample mean is lower than the sliding mean of one std (*STandard Deviation*) and remove eventually the specific channel:

$$ if \quad \overline{Bt_i(\nu)} \leq \widetilde{Bt_i(\nu)} - std \quad then \quad Bt_i(\nu) \quad is \quad removed \tag{17} $$

where $\overline{Bt_i(\nu)}$ is the sample mean of the entire i-th class, $\widetilde{Bt_i(\nu)}$ is the sliding mean and std is the standard deviation of the sliding mean. As pointed out in the formula the mean values are channel but also class dependent, so might happen that for a class a particular channel is removed while for the other it's not. To improve the consistency in this aspect, the procedure has been applied to all the classes and then the one with the biggest variability (std) has been taken as reference. In our case the *ASFALTO* class (AS) is the one taken as reference, the results of this procedure are presented in fig.28. This method coupled with the cut off reduced the spectra from 11.201 channels to 644 allowing to perform a complete classification in a reasonable time, generally under 15 minutes.

This procedure has demonstrated to be essential for a correct classification. In fact, during the construction of the training set, the first classification tried applied only the spectral reduction between 750-1100 cm^{-1} and 1100-1200 cm^{-1} with the sampling 1:8 of the channels available, for a total of 701 channels left. With just this selection the algorithm is unable to sort the pixels in the images and gives a not classified results for all of them.

(a)   (b)
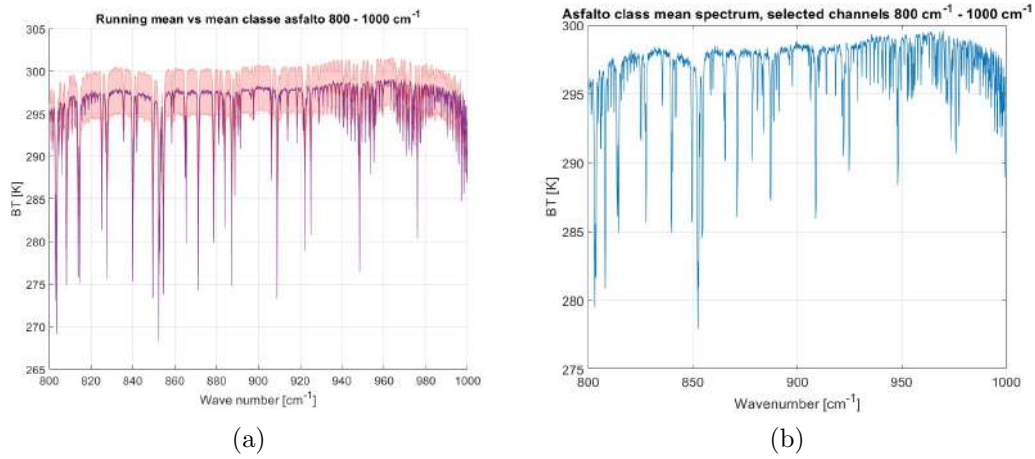
Figure 28: a) superposition of the simple mean (blue line) and 11 channels sliding mean ± std (red lines and shading) for the $ASFALTO$ class, only the 800 - 1000 cm^{-1} spectral interval is plotted b) remaining spectrum after the absorption lines elimination step
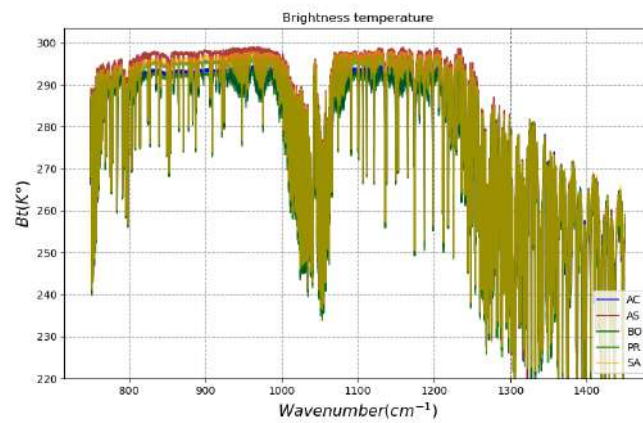

Figure 29: Mean brightness temperature $B_t(\nu)$ computed for each training set in surface classification

4.5.3 CIC soil classification results

As done for the the cloud classification, the performances of the CIC classifier have been tested on a series of images to see if the classification is correct and what are the overall behaviour. The selection has been made in such a way that allows a test with each possible terrain, also with different combination between them. To improve the performances the CIC algorithm with the double metric approach has been utilized for this classification and three different classes are used in training of the algorithm.

Granule	classes utilized and counts		
19:18:48	AC 2291	PR 269	SA 2107
19:19:02	AC 1666	PR 197	BO 1530
19:37:48	AC 520	PR 318	BO 3736
19:59:13	AS 954	PR 1535	BO 2055

Table 10: table containing each granule in the test set (first column) and the classes utilized for the classification with the corresponding number of occurrences in each image

Starting from the image at 19:18:48 the results are able do discriminate the two different areas: one is the lake and the other is the soil which is identified as a sand area. The edge of the lake is not well positioned and some dubious area are presented, both in the sand areas as well as in the lake section. The presence of miss classified objects are expected looking to the mean brightness temperature profile since the difference are barely visible and none of the spectra present unique features; Nevertheless, the algorithm has still been able to separate the two areas present in the image.

The classification make for the granule collected at 19:37:48 shows a really good agreement with the area pictured by the GoPro. Both the river and the small green area next to it are present, their edges are very precise and the shape are exact. Looking at the main spectra for each class the separation between the grass class and the water is way more evident. On the other hand, the forest (BO) mean spectra is really close to the water one and this might explain the miss classification around the central area of the image.

For the granule collected at the 19:19:02 a similar scenario to the scene acquired at 19:18:48 is found. The location is very close to the previous one since they've been acquired with just 14 seconds gap, but we decide to operate the classification with the class BO instead of SA to see if this one improves the results with respect to the previous
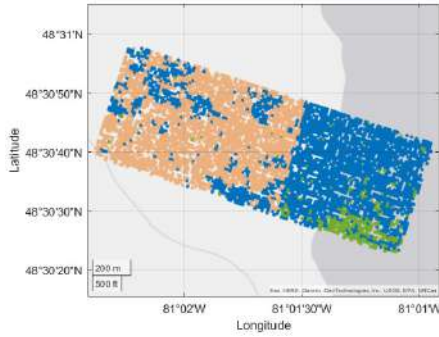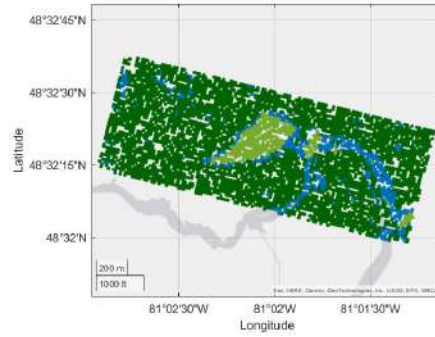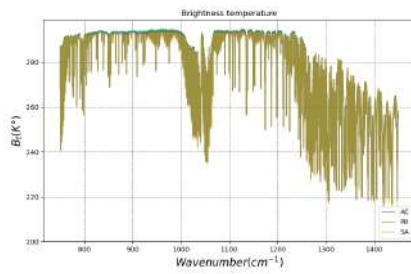
Figure 30: In the left column: a) CIC surface classification for granule collected at 19:18:48; c) brightness temperature spectral mean $Bt(\nu)$ for the 3 different classes: AC (blue), SA (orange) and PR (light green) e) GoPro image taken at 19:18:50 on Aug:23, the yellow represent approximately the granule area. In the right column: a) CIC surface classification for granule collected at 19:37:48; c) brightness temperature spectral mean $Bt(\nu)$ for the 3 different classes: AC (blue), BO (dark green) and PR (light green) e) GoPro image taken at 19:37:50 on Aug:23, the yellow represent approximately the granule area.

50

one. This seems reasonable looking at the GoPro image which display a consistent area with high vegetation(fig.31(e)). A fraction of the lake is correctly located from the algorithm (upper right), but there are a lot of miss classified object on the soil, where there is the presence a huge area identified as water. Also, in this case seems that the class BO and AC might be overlapped and the algorithm has some difficulties in discriminate between the two.

The last image analyzed is taken at the 19:59:13 when the balloon flew over a small urban area where streets and buildings were present. For this reason the classes utilized in this case are AS,BO,PR. The purpose is to highlight urbanized areas and sees if they're distinguishable from the natural environment. The image has been classified respecting the variety of shapes and elements in it with just a few dubious element between PR and AS. This might also be attributable to the presence bright areas which the CIC has identified as an antrophogenic source. The area on the left side of the image is really difficult to categorize since the streets and green areas are distributed on very small spaces and the separation between them is really thin. In this case the classifier returns a correct shape of the objects, the presence of streets and vegetation is consistent with the GoPro image.
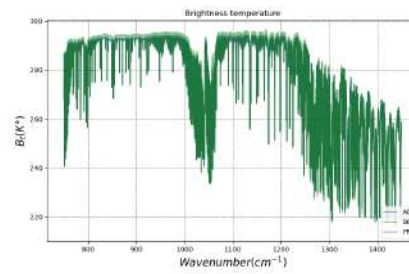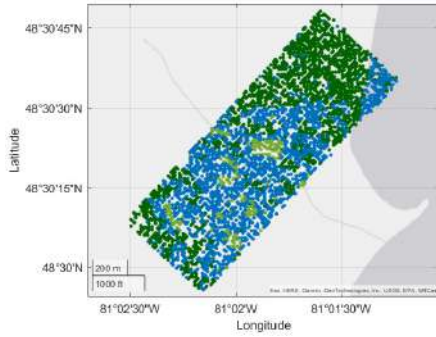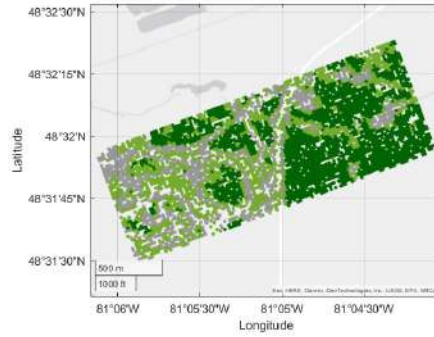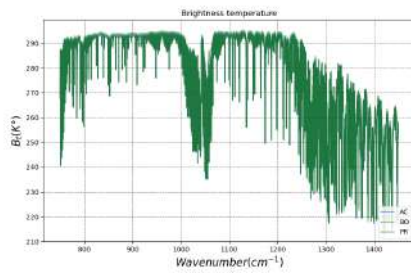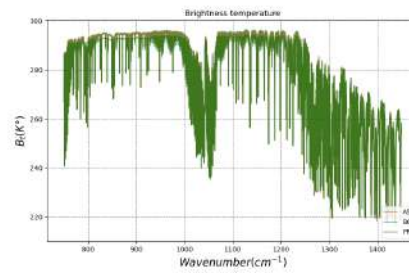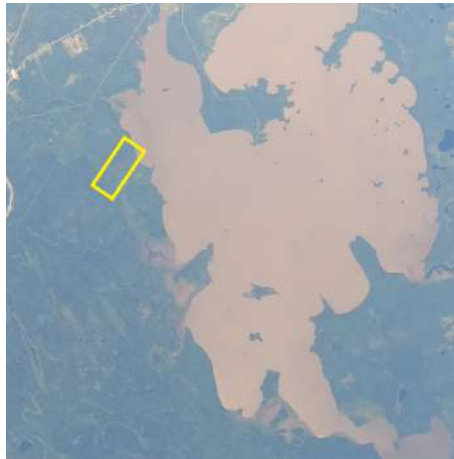
Figure 31: In the left column: a) CIC surface classification for granule collected at 19:19:02; c) brightness temperature spectral mean $Bt(\nu)$ for the 3 different classes: AC (blue), BO (dark green) and PR (light green) e) GoPro image taken at 19:19:00 on Aug:23, the yellow represent approximately the granule area. In the right column: a) CIC surface classification for granule collected at 19:59:13; c) brightness temperature spectral mean $Bt(\nu)$ for the 3 different classes: AS (grey), BO (dark green) and PR (light green); e) GoPro image taken at 19:59:10 on Aug:23, the yellow represent approximately the granule area.

52

5 FARM analyses and results

5.1 Clear sky retrival

In this section the results of the retrieval on the granule collected at the 19:48:18 are presented. All the following results have been obtained thanks to the FARM code for a clear sky scenario so the presence of clouds is not taken into account. The state vector utilized for this first test is composed of: spectral radiance (Rad) and it's noise (δRad), temperature vertical profile T(p), the vertical profile of H_2O and the surface emission coefficient (ϵ). All this quantity have been derived for each different surface class present in the classification with the purpose to see if differences occurs and in which variable of the state vector. For example, if the soil classification has worked as intended different values for the emissivity should be found since it changes between a high and flourish vegetation (such as a forest), to a grass field, to a lake. If this difference is really present, this information can be utilized to give a even more precise a priori information to the FARM, allowing to select better first guess for the retrieval based on the different type of soil under analyses.

To perform the retrieval, a series of input are required from the code to work properly. We list here all the different information:

1. input radiance in nw/cm^2cmstr and the spectral interval desired. In our case, this is the mean of all the pixel sorted from the CIC as a specific type of soil. To keep a reasonable computation time and still been able to observe what we're interested in, has been kept only the atmospheric window from 750-1000 cm^-1;

2. the 'a priori' information about the state of the atmosphere which is given, in our case, from the ERA5 reanalyses for the day under exam Aug. 23 2022 at 18. This file contains the gas concentration and temperature vertical profile for all the species required from the rtm(*Radiative transfer Model*) to work properly;

3. the 'a priori' information about the emissivity which is set at first to a uniform value for all the classes equal to 0.85 ± 0.1. This is the parameter to improve after the retrieval since different sources, in our case soil types, should have different emissivity profile.

4. the clouds profile but for our analyses this is not required because there are no clouds in the image;

5. the covariance matrix for the instrumental noise. This matrix contain information about the correlation of different channels' noise; it's a diagonal matrix containing the spectral variance plus a few off-diagonal elements related to the correlation between channels. This correlation is inevitably introduce from the instrument and
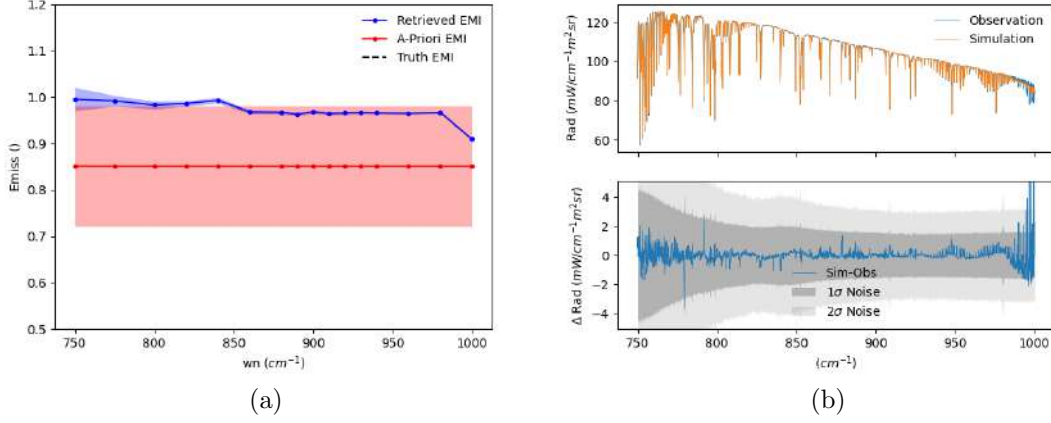
Figure 32: a) Emissivity retrieved value for the class AC (water) with associated error (shaded bar = 1σ), degree of freedom = 15.8; b) observed spectral radiance vs simulated spectral radiance $(mW/(m^2 cmsr))$ (above) and their residual compared with the 1σ threshold (below)

from the post processing. This information is usually related to a single measure but in our case we're looking at a mean of different pixels data. For this reason a diagonal matrix has been utilized with element equal to the spectral variance for each channel, assuming that the channels are uncorrelated.

6. a spectral grid necessary to identify at which wave number the emission coefficient has to be computed with it's own associated error. In our case the grid is not equally spaced but we have a better resolution in the window area 850-950 cm^{-1}.

7. a vertical grid for the retrieval of gas concentration and temperature profile.

5.1.1 Surface emissivity (ϵ) and Spectral radiance (RD) retrieval

The surface emissivity results are presented here next to the retrieval for the spectral radiance. The results have been separated for each classes obtained from the surface CIC classification on the granule collected at 19:18:48. In the following images is present in labels a voice dedicated to the truth profile, usually display in black, that has not to be considered since to objective thruth is provided for this observation. Only the emissivity is compared with a reference value displayed in figure 34.

The emissivity (ϵ) is almost identical for the water (AC) and the grass (PR) with an absolute value close to 1 along almost all the spectral range. There is a a drop in the ϵ value, shared from both the classes, after 950 cm^{-1} bringing ϵ closer to 0.9. The values obtained for the class sand (SA), even if the overall behaviour of the previous two
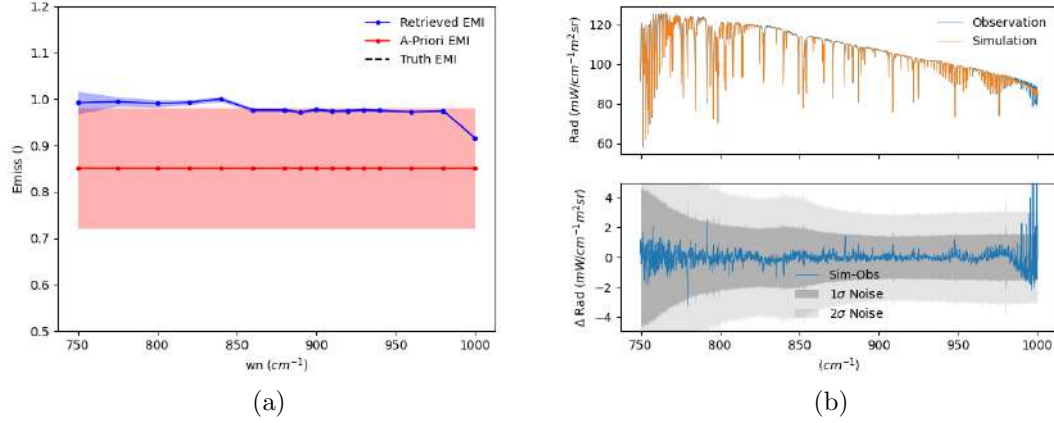
Figure 33: a) Emissivity retrieved value for the class PR (grass) with associated error (shaded bar $= 1\sigma$), degree of freedom $= 15.8$; b) observed spectral radiance vs simulated spectral radiance (mw/m^2cmsr) (above) and their residual compared with the 1σ threshold (below)

classes is preserved, the absolute value are smaller and there is a first drop after 850 cm^{-1} and the second one brings it bellow 0.9 . This values are consistent with previously obtained results (Huang et al.2016 [17]) and the associated error is really small. Bigger uncertainties are present in the values around the 750 cm^-1 which is where the spectral radiance has significant oscillations due to the presence of the absorption band of CO_2 centered at 667 cm^{-1}. The number of degree of freedom is 15.8 for the emissivity results.

To give a comparison for the retrieval emissivity results, is shown in figure 34 the complete shape of $\epsilon()$ profiled as obtained from Huang.

For what concerns the spectral radaince features, they are reproduced from the RTM with differences between the model and the observation bellow the 1σ boundary. Only the last section of the spectra, from 970 cm^{-1} and above shows significative difference between the two which becomes more and more evident as we progress towards the right boundary. This section is where the absorption of the ozone O_3 starts, with the middle of its absorption band located at 1052 cm^{-1}. The differences between the 3 spectral radiance profile for the 3 classes are very small and is not possible to distinguish particular features in anyone of this.
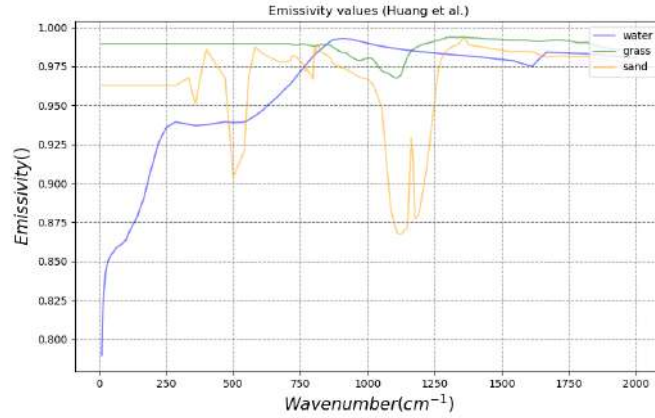
Figure 34: Complete emissivity profile obtained from Huang et al.2016 [17]

(a)   (b)
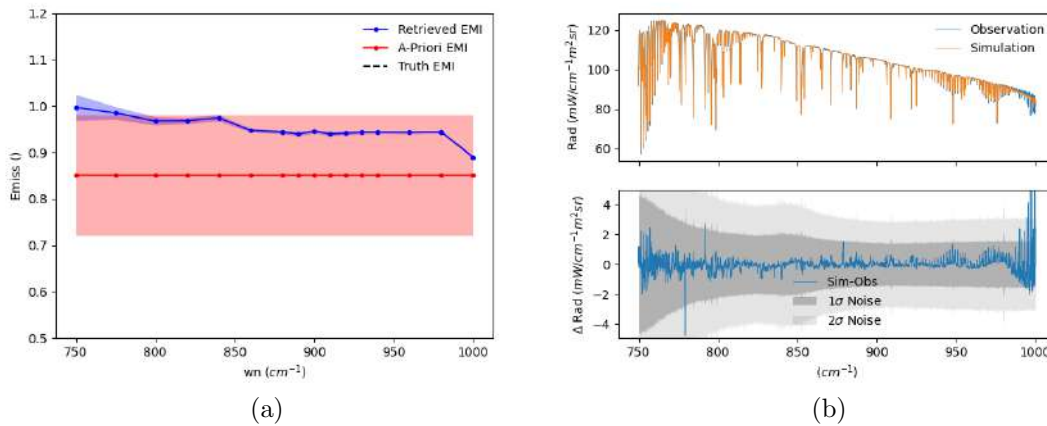
Figure 35: a) Emissivity retrieved value for the class AC (water) with associated error (shaded bar = 1σ), degree of freedom = 15.8; b) observed spectral radiance vs simulated spectral radiance (mw/m^2cmsr) (above) and their residual compared with the 1σ threshold (below)

5.1.2 Temperature profile and H_2O profile retrieval

This section is dedicated to the retrieval results for the vertical profile of both temperature and humidity. As for the emissivity and the radiance we present separately the results for each classes identify during the surface classification.

Starting from the temperature vertical profile the differences between the 'a priori' and the simulation are very small and way bellow the $1\ \sigma$ threshold. The negative vertical

gradient of T is clearly visible as well the inversion on the top of the atmosphere where the results seems to overestimate the value of T. Also the difference between the three retrieved profile are minimum, the sand is the only one which seems to posses a little shift with respect to the other two. The number of degree of freedom for this results is 1.9.

For what concerns the H_2O profile some discrepancies between classes and also with respect to each other are present. The retrieved profile are always bellow or at the the edge of the 1σ threshold, a small underestimation along the all atmospheric column of the H_2O content is present. Still, the profile shape is respected and the SA class is the closest to the 'a priori'. This profile of H_2O has also a small inversion near the surface.

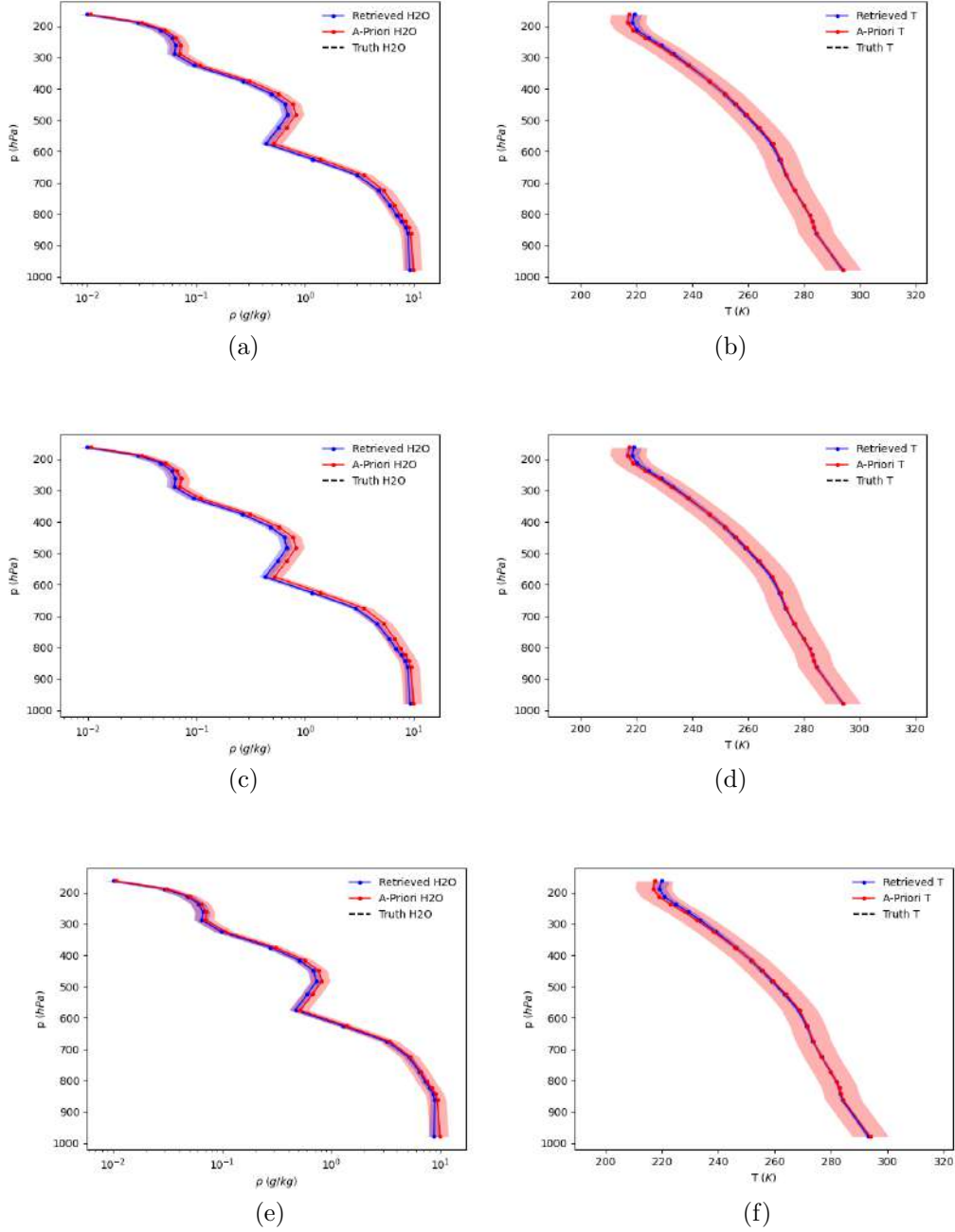Figure 36: In the left column: retrieved values for the H_20 concentration (g/Kg) for the 3 different classes with associated error 1σ: a) AC water; c) PR grass; e) SA sand, number of degree of freedom = 1. In the right column: the temperature vertical profile retrieval results (K°) with the associated error 1σ: b) AC water; d) PR grass; f) SA sand, number of degree of freedom = 1.9.

6 Concluding remarks

In this last section a summary of the work is provided.

The study aimed at analysisng data from the HEMERA field campaign held in Timmins (Canada) in the summer of 2022. Unfortunately, observations collected by the FORUM prototype called FIRMOS have been compromised from unexpected issue due to the a pump vibration propagation. FIRMOS data are still under level 1 analyses in a tentative to limit the disturbances added by the gondola vibration which are particularly strong in the radiance signal.

Additionally we dealt with rotation of the instrument around the vertical axes and the premature descent of the balloon during the flight. Nevertheless, all data from the GLORIA sensor (prototype of the ESA CAIRT mission) have been made available and thus the nadir observations could be correctly geolocated. Results concerning the GLORIA data underline the performances of this instrument also at NADIR. In particular, the implementation of the cloud identification and classification algorithm (CIC) on such a high resolution spatial grid has allowed to perform different and innovative analysis. The results are consistent with the observation and also with other methods like the k-means clustering. The hit score for the classifier in this analyses exceed the 90 % and confirms the quality of the results. Furthermore, the ability to separate within the same cloud different areas with potentially different optical depths could lead to really important results. For examples a further implementation could be the analyses with FARM of the different section of the cloud to see if differences in composition, ice water content (IWC), liquid water content (LWC) are present.

CIC has also obtained consistent results in the surface classification where the hit scores gives multiple results based on the classes utilized but without going bellow the 0.667 accuracy. In this context, CIC has demonstrated to be way more performing than a regular threshold method since, even with so small differences between the brightness temperature, the classification was able to describe with a high accuracy the observed scene. Is also necessary to point out that this types of analyses are usually executed in different section of the spectra (Short Wave), where the instrument FOV can be more tight, allowing for a better precision and a bigger section of the spectra can be analysed. Being able to obtain this results in this section of the spectra is a important results and leaves space for further implementation

The results obtained with the FARM code are also important. The code is able to resolve differences in emissivity even with such small variation between the spectra, reporting consistent result with previously obtained emisisvity profile. The high number of degree of freedom is also important because confirm the addition of a substantial amount of information with respect to the first guess.

The retrieved profile for H_2O and T converge with the first guess values but without adding a lot of information given that the degree of freedom are, respectively, 1 and 1.9.

Still, the results are important since this is the first time that FARM is applyed to non simulated data and the performance are as espceted.

References

[1] IPCC, 2023: Climate Change 2023: Synthesis Report. Contribution of Working Groups I, II and III to the Sixth Assessment Report of the Intergovernmental Panel on Climate Change [Core Writing Team, H. Lee and J. Romero (eds.)]. IPCC, Geneva, Switzerland, 184 pp., doi: 10.59327/IPCC/AR6-9789291691647

[2] Palchetti, L., Belotti, C., Bianchini, G., Castagnoli, F., Carli, B., Cortesi, U., Pellegrini, M., Camy-Peyret, C., Jeseck, P., and Té, Y.: Technical note: First spectral measurement of the Earth's upwelling emission using an uncooled wideband Fourier transform spectrometer, Atmos. Chem. Phys., 6, 5025–5030, https://doi.org/10.5194/acp-6-5025-2006, 2006.

[3] Martin G. Mlynczak, David G. Johnson, Harri Latvakoski, Kenneth Jucks, Mike Watson, David P. Kratz, Gail Bingham, Wesley A. Traub, Stanley J. Wellard, Charles R. Hyde, Xu Liu: First light from the Far-Infrared Spectroscopy of the Troposphere (FIRST) instrument, Geophysical research Letters, vol.33, issue 7, https://doi.org/10.1029/2005GL025114

[4] Maestri, T., Rizzi, R., Tosi, E., Veglio, P., Palchetti, L., Bian- chini, G., Di Girolamo, P., Masiello, G., Serio, C., and Summa, D.: Analysis of cirrus cloud spectral signatures in the far infrared, J. Quant. Spectrosc. Ra., 141, 49–64, https://doi.org/10.1016/j.jqsrt.2014.02.030, 2014

[5] Belotti, C., Barbara, F., Barucci, M., Bianchini, G., D'Amato, F., Del Bianco, S., Di Natale, G., Gai, M., Montori, A., Pratesi, F., Rettinger, M., Rolf, C., Sussmann, R., Trickl, T., Viciani, S., Vogelmann, H., and Palchetti, L.: The Far-Infrared Radiation Mobile Observation System (FIRMOS) for spectral characterization of the atmospheric emission, Atmos. Meas. Tech., 16, 2511–2529, https://doi.org/10.5194/amt-16-2511-2023, 2023.

[6] Friedl-Vallon F., Gulde, T., Hase, F., Kleinert, A., Kulessa, T., Maucher, G., Neubert, T., Olschewski, F., Piesch, C., Preusse, P., Rongen, H., Sartorius, C., Schneider, H., Schönfeld, A., Tan, V., Bayer, N., Blank, J., Dapp, R., Ebersoldt, A., Fischer, H., Graf, F., Guggenmoser, T., Höpfner, M., Kaufmann, M., Kretschmer, E., Latzko, T., Nordmeyer, H., Oelhaf, H., Orphal, J., Riese, M., Schardt, G., Schillings, J., Sha, M. K., Suminska-Ebersoldt, O., and Ungermann, J.: Instrument concept of the imaging Fourier transform spectrometer GLORIA, Atmos. Meas. Tech., 7, 3565–3577, https://doi.org/10.5194/amt-7-3565-2014, 2014.

[7] James W. Brault, "New approach to high-precision Fourier transform spectrometer design," Appl. Opt. 35, 2891-2896 (1996)

[9] D. K. Zhou et al., "Global Land Surface Emissivity Retrieved From Satellite Ultraspectral IR Measurements," in IEEE Transactions on Geoscience and Remote Sensing, vol. 49, no. 4, pp. 1277-1290, April 2011, doi: 10.1109/TGRS.2010.2051036.

[10] https://www.esa.int/Applications/Observing_the_Earth/FutureEO/FORUM

[11] Riese, M., Oelhaf, H., Preusse, P., Blank, J., Ern, M., Friedl-Vallon, F., Fischer, H., Guggenmoser, T., Höpfner, M., Hoor, P., Kaufmann, M., Orphal, J., Plöger, F., Spang, R., Suminska-Ebersoldt, O., Ungermann, J., Vogel, B., and Woiwode, W.: Gimballed Limb Observer for Radiance Imaging of the Atmosphere (GLORIA) scientific objectives, Atmos. Meas. Tech., 7, 1915–1928, https://doi.org/10.5194/amt-7-1915-2014, 2014.

[12] Magurno, D.; Cossich, W.; Maestri, T.; Bantges, R.; Brindley, H.; Fox, S.; Harlow, C.; Murray, J.; Pickering, J.; Warwick, L.; et al. Cirrus Cloud Identification from Airborne Far-Infrared and Mid-Infrared Spectra. Remote Sens. 2020, 12, 2097. https://doi.org/10.3390/rs12132097

[13] Cossich, W., Maestri, T., Magurno, D., Martinazzo, M., Di Natale, G., Palchetti, L., Bianchini, G., and Del Guasta, M.: Ice and mixed-phase cloud statistics on the Antarctic Plateau, Atmos. Chem. Phys., 21, 13811–13833, https://doi.org/10.5194/acp-21-13811-2021, 2021.

[14] https://www.esa.int/Applications/Observing_the_Earth/FutureEO/Preparing_for_tomorrow/... .. Four_mission_ideas_to_compete_for_Earth_Explorer_11

[15] Henry E. Revercomb, H. Buijs, Hugh B. Howell, D. D. LaPorte, William L. Smith, and L. A. Sromovsky, "Radiometric calibration of IR Fourier transform spectrometers: solution to a problem with the High-Resolution Interferometer Sounder," Appl. Opt. 27, 3210-3218 (1988)

[16] Mittal, H., Pandey, A.C., Saraswat, M. et al. A comprehensive survey of image segmentation: clustering methods, performance parameters, and benchmark datasets. Multimed Tools Appl 81, 35001–35026 (2022). https://doi.org/10.1007/s11042-021-10594-9

[17] Huang et al.,An observationally based global band-by-band surface emissivity dataset for climate and weather simulations,JAS, 73, 3541-3555, doi:10.1175/JAS-D-15-0355.1, 2016.